A possible high-temperature origin of the Moon and its geochemical consequences

E.S. Steenstra[1-3*], J. Berndt[3], S. Klemme[3], Y. Fei[1], W. van Westrenen[2]

[1] The Earth and Planets Laboratory, Carnegie Institution for Science, Washington D.C., U.S.A.

[2] Faculty of Science, VU Amsterdam, Amsterdam, The Netherlands

[3] Institute of Mineralogy, University of Münster, Münster, Germany

*Corresponding author email address: esteenstra@carnegiescience.edu

---

Abstract. The formation of the Moon is thought to be the result of a giant impact between a Mercury-to-proto-Earth-sized body and the proto-Earth. However, the initial thermal state of the Moon following its accretion is not well constrained by geochemical data. Here, we provide geochemical evidence that supports a high-temperature origin of the Moon by performing high-temperature (1973–2873 K) metal-silicate partitioning experiments, simulating core formation in the newly-formed Moon. Results indicate that the observed lunar mantle depletions of Ni and Co record extreme temperatures (>2600–3700 K depending on assumptions about the composition of the lunar core) during lunar core formation. This temperature range is within range of the modeled silicate evaporation buffer in a synestia-type environment. Our results provide independent geochemical support for a giant-impact origin of the Moon and show that lunar thermal models should start with a fully molten Moon. Our results also provide quantitative constraints on the effects of high-temperature lunar differentiation on the lunar mantle geochemistry of volatile, and potentially siderophile elements Cu, Zn, Ga, Ge, Se, Sn, Cd, In, Te and Pb. At the extreme temperatures recorded by Ni and Co, many of these elements behave

insufficiently siderophile to explain their depletions by core formation only, consistent with the inferred volatility-related loss of Cr, Cu, Zn, Ga and Sn during the Moon-forming event and/or subsequent magma-ocean degassing.

Keywords: *Moon, Core formation, Giant Impact, Siderophile, Accretion, Volatiles*

---

1. INTRODUCTION

The giant impact model of Moon formation is predominantly studied with hydrodynamic simulations (Cameron and Ward, 1976; Benz et al., 1986; Canup, 2012; Cuk et al., 2016; Lock et al., 2018). Several groups have specifically studied the evolution of the Moon-forming material following the giant impact (Charnoz and Michaut, 2015; Lock et al., 2018; Nakajima and Stevenson, 2018), and suggest that initial temperatures of this material are extremely high. The thermochemical models in Nakajima and Stevenson (2018) suggest that peak temperatures within the mid-plane disk could have been up to 4000–4500 K. On the other hand, Rufu et al. (2017) suggested that the Moon could have been formed by a succession of smaller impacts on the proto-Earth, which would likely result in lower peak temperatures of Moon-forming materials. The most recent lunar formation models suggest the Moon formed in a cloud of vaporized rock moving at a high angular momentum formed directly after a high-energy impact between the proto-Earth and the impactor (Lock et al., 2018).

Geochemical evidence for the conditions accompanying a giant impact is qualitative at present. The strongest geochemical evidence for the occurrence of a Moon-forming giant impact stems from measurements of very small but detectable differences in the isotopic composition of volatile elements between primitive lunar materials and terrestrial

samples (Paniello et al., 2012; Wang and Jacobsen, 2016; Kato and Moynier, 2017; Pringle et al., 2017). Although their isotopic compositions in lunar samples provide fundamental clues to the ambient thermal regime at some stage of lunar formation, these geochemical data do not provide specific constraints on the thermal state of the Moon directly *after* the Moon-forming event. For some of these elements their isotopic compositions may have been altered in much later stages during lunar evolution (Paniello et al., 2012; Kato and Moynier, 2017; Sossi et al., 2018), e.g., during crystallization of the lunar magma ocean (LMO). For example, chromium isotopic compositions of primitive lunar rocks have been used to argue for low-temperature degassing of Cr following formation of the Moon (Sossi et al., 2018), whereas models for other isotopic systems (e.g., Wang and Jacobsen, 2016) have been used to support the hypothesis of a very hot (i.e., > 3500 K) origin of the Moon (Lock et al., 2018).

Current estimates of early Moon temperatures range from cool enough to only enable shallow, partial melting, to sufficiently high to lead to whole-Moon melting (e.g., Longhi, 2006; Steenstra et al., 2016; Charlier et al., 2018). Some experimental studies of LMO crystallization have been used to argue for shallow melting (Charlier et al., 2018), but the outcome of these models depends strongly on a variety of assumptions, including the efficiency of crystal-melt separation, water content in the LMO and crystallization regime (Lin et al., 2016; Charlier et al., 2018; Rapp and Draper 2018).

Here, we attempt to constrain temperatures in the early Moon by assessing the temperatures during core formation, which is the first major differentiation event in the Moon after its accretion. To this end we performed high-temperature (1973–2873 K) metal-silicate partitioning experiments at high pressure, simulating core formation in the

newly-formed Moon, and assessing the core-mantle distribution of a range of non-volatile and volatile siderophile trace elements (Ni, Co, Cu, Zn, Ga, Ge, Se, Sn, Cd, In, Te and Pb).

Siderophile elements have been shown to be a valuable tool for studying the thermal regime during the earliest differentiation of the Earth (e.g., Wade and Wood, 2005) and other planetary bodies (e.g., Chabot and Agee, 2003). Previous siderophile element studies related to the Moon generally assumed a significant impactor contribution to the lunar siderophile element budget (O'Neill et al., 1991; Rai and van Westrenen, 2014; Steenstra et al., 2016), but to date definitive geochemical evidence to support such a contribution has not been found (e.g., Kruijer et al., 2015). On the other hand, multiple elemental and isotopic lines of evidence indicate a bulk silicate Earth (BSE) - like bulk Moon composition, at least in terms of non-volatile elements (e.g., Ti, Zhang et al., 2012; W, Kruijer et al., 2015; O, Young et al., 2016). A strong geochemical link between the BSE and the bulk Moon is also inferred from current ideas and dynamical models of lunar formation (Canup , 2012; Cuk and Stewart, 2012; Lock et al., 2018), isotopic similarities of refractory elements between BSE and bulk Moon (e.g., O, Ti, Fe, W; Zhang et al., 2012; Kruijer et al., 2015; Young et al., 2016; Sossi and Moynier, 2017) and similarity in abundances of major and trace elements between the BSE and BM, including virtually the whole class of refractory lithophile elements (Dauphas et al., 2014).

Here, we leverage this equality between bulk Moon and BSE composition for refractory elements to estimate the temperature during core formation in the Moon, using the elements Ni and Co. It is well established that these elements are depleted in the lunar mantle relative to BSE (Delano, 1986; Jones and Palme, 2000; Sossi et al., 2018).

However, their depletions are much smaller than expected given their siderophile behavior at temperatures of up to ~2000 K (Kegler et al., 2008; Siebert et al., 2011), especially given that the lunar core is likely to be sulfur-poor (Righter et al., 2017; Steenstra et al., 2018; Brenan et al., 2019). Previous metal liquid-silicate melt partitioning experiments have shown that the siderophile behavior of Co and Ni is affected by changes in pressure and temperature (*P*-*T*), whereas it is largely unaffected by changes in silicate melt composition and oxygen fugacity (fO_2) given their 2+ valence states (Thibault and Walter, 1995; Kegler et al., 2008; Siebert et al., 2011). Due to their non-volatile nature, Ni and Co abundances in the Moon are unlikely to have been significantly affected by volatility-related fractionation processes. In contrast to other non-volatile elements such as the highly siderophile elements, the high abundances of Co and Ni in the lunar mantle exclude significant disturbance of their concentrations through addition of a late veneer significantly post-dating Moon formation. Their metal-silicate partitioning behavior is likely unaffected by changes in silicate melt composition, in contrast to other refractory elements such as Mo and W (Kegler et al., 2008; Siebert et al., 2011; Steenstra et al., 2017a). Given the 2+ valence state of Co and Ni under lunar-relevant fO_2, the relative depletions and ratios of these elements are independent of the fO_2 during lunar differentiation (e.g., Siebert et al., 2011). The depletions of Ni and Co in the lunar mantle therefore provide a unique opportunity to constrain the initial thermal state of the Moon during core formation. Using our Ni and Co-based models, we also assessed to what extent the lunar mantle depletions of the other, more volatile and potentially siderophile elements could reflect high-temperature lunar core formation.

2. METHODS

2.1 Experimental approach

To better constrain the effect of temperature on the metal liquid-silicate melt partition coefficients of Co, Ni and a variety of other trace elements for lunar silicate melt compositions, we performed high-pressure, high-temperature experiments in a 1500-ton multi-anvil apparatus at the Geophysical Laboratory, Carnegie Institution for Science at temperatures between 1973 and 2873 K and pressures of 3.2–3.9 GPa (Table 1). Experiments were conducted using 18mm edge length Cr-doped MgO or ZrO_2 octahedra, graphite heaters and polycrystalline 1.6 mm I.D. MgO capsules. Capsules were loaded with a synthetic powdered analogue of primitive lunar Apollo 15 green glass (Delano, 1986) and Fe metal doped with a range of trace elements, mixed in a volume 2:1 ratio. Two metal compositions were used (see Table 1).

Samples were pressurized to peak pressures before heating. Pressure calibration was based on the qtz-coes and gt-pv transitions, resulting in an estimated pressure uncertainty of ~0.2 GPa. Temperature was monitored using a Type C (95%W/5%Re - 74%W/26%Re) thermocouple placed directly above the sample container at the assembly hotspot. Metal-silicate mixtures were sintered at 1273 K for 60 to 120 min to reduce porosity of the MgO capsule, and subsequently heated to target temperature. Above 2473 K, experimental temperatures were estimated using well-defined power-temperature relationships (Appendix section A.1; Fig. S.1). Experiments were run at peak conditions between 10 and 0.5 min, depending on final temperature. Although no time-series was performed, these run durations have previously been shown to be sufficient for attainment of metal liquid-silicate melt equilibrium at these extreme temperatures (Thibault and Walter, 1995; Wade and Wood, 2005; Siebert et al., 2011). Experiments were rapidly

quenched by shutting off the power to the furnace. Recovered samples were mounted in petropoxy resin, polished using different grades of Al polishing powder and analyzed using EPMA and laser ablation ICPMS (inductively coupled plasma mass spectrometry) techniques.

2.2 Analytical approach

Major element abundances of metals and silicates were determined using JEOL JXA-8530F electron probe microanalyses at the University of Münster, Germany and at the Dutch National Geological Facility at Utrecht University, and are summarized in Tables S.1 and S.2. Metal alloys and silicate melts were analyzed with a defocused 15 µm diameter beam. The analyses were done using beam currents of 20 nA and an accelerating voltage of 15 kV. Counting times were 30 s for peak and 15 s for background for major elements. Measurement points were set in lines and/or raster grids, depending of the available surface area of the analysed phases, with step sizes approximately equivalent to spot sizes. A set of synthetic and natural silicate and metal reference materials were used for standardization. Data reduction was performed using the $\Phi(\rho Z)$ correction. Additional details related to the EPMA analyses are provided in Appendix section A.2.

LA-ICP-MS analyses were performed at the University of Münster to quantify the abundances of trace elements in the metal liquids and silicate melts (Tables S.1, S.2). Analyses were performed using a 193 nm ArF excimer laser (Analyte G2, Photon Machines) with a repetition rate of 10 Hz and energy of ~3–4 J/cm^2 throughout the entire analytical session with beam diameters ranging between 25–50 µm. The following

isotopes were measured: ^{29}Si, ^{31}P, ^{43}Ca, ^{49}Ti, ^{51}V, ^{53}Cr, ^{55}Mn, ^{59}Co, ^{60}Ni, ^{61}Ni, ^{63}Cu, ^{66}Zn, ^{69}Ga, ^{73}Ge, ^{75}As, ^{82}Se, ^{93}Nb, ^{95}Mo, ^{118}Sn, ^{121}Sb, ^{125}Te, ^{181}Ta, ^{182}W and ^{208}Pb. The NIST 612 glass was used as an external reference material for both metal alloys and silicate melts. Concentrations of Si in the silicate melt and Ni in the metallic liquid were used as internal standards. The USGS reference materials BIR-1G and BCR-2G were analyzed every ~20 LA-ICP-MS spots to assess the analytical accuracy and precision of measured trace element concentrations (Fig. S.2).

The use of non-matrix-matched primary standards requires corrections on measured concentrations of volatile and highly refractory elements in metals. Steenstra et al. (2019) showed that the extent of elemental fractionation during LA-ICP-MS of iron-rich metal analyses is most significant for the most volatile (e.g., Se, Te, Cd, Pb) and most refractory elements (i.e., Mo, W). Neglecting these matrix effects would result in significant overestimation of the $\mathrm{D_i^{met\ liq-sil\ melt}}$ values. Abundances of volatile elements in metals were therefore corrected downwards using the empirical correction factors reported in the latter study (Steenstra et al., 2019).

3. RESULTS

3.1 Run products and metal liquid-silicate melt partition coefficients

Run products show well-segregated metallic blobs in a quenched silicate melt (Fig. 1). All silicate melts quenched to a heterogeneous phase with spinifex olivine crystals and interstitial glass. Ferropericlase crystals (Mg,Fe)O were commonly formed due to the increase of the MgO content of the silicate melt through interaction of the silicate melt with the MgO capsule at high temperature conditions. The increase of the silicate melt

MgO content due to capsule interaction also resulted in a substantial decrease of CaO and Al_2O_3 contents, compared to the initial starting composition (Fig. S.4). No evidence for metal zoning was observed, although smaller-scale (<5–10 um) heterogeneities were observed, as typically observed for quenched metal alloys.

Metal liquid-silicate melt partition coefficients of Co, Ni and the other trace elements were treated as exchange coefficients by considering the following equilibria (e.g., Wade and Wood, 2005):

$$\mathrm{MO}_{n/2}^{\mathrm{silicate}} + \frac{n}{2}\mathrm{Fe}^{\mathrm{metal}} = \frac{n}{2}\mathrm{FeO}^{\mathrm{silicate}} + \mathrm{M}^{\mathrm{metal}} \quad (1)$$

where M or MO is the element or oxide considered with its corresponding valence *n*. Taking the logarithm of the equilibrium constant ($K_{\mathrm{app}}^{\mathrm{met\ liq-sil\ melt}}$) results in Eq. (2):

$$\log K_{\mathrm{app}}^{\mathrm{met\ liq-sil\ melt}} = \log\frac{(x_{\mathrm{FeO}}^{\mathrm{sil\ melt}})^{n/2}\cdot(x_{\mathrm{M}}^{\mathrm{met\ liq}})}{(x_{\mathrm{MO}_{n/2}}^{\mathrm{sil\ melt}})\cdot(x_{\mathrm{Fe}}^{\mathrm{met\ liq}})^{n/2}} + \log\frac{(\gamma_{\mathrm{M}}^{\mathrm{met\ liq}})}{(\gamma_{\mathrm{Fe}}^{\mathrm{met\ liq}})^{n/2}} + \log\frac{(\gamma_{\mathrm{FeO}}^{\mathrm{sil\ melt}})^{n/2}}{(\gamma_{\mathrm{MO}_{n/2}}^{\mathrm{sil\ melt}})} \quad (2)$$

where *x* are molar fractions, *n* is the valence of the element considered and γ are the activity coefficients of Fe and trace element *M.* Valences were assumed to be 1+ for Cu, 2+ for Ni, Co, Cr, Zn, Ge, Cd, Sn, Pb and 3+ for Ga and In (e.g., Siebert et al., 2011). Note that the above approach directly accounts for variable fO_2 between the experiments. Activity coefficients of Ni, Co and Cr in the metal ($\gamma_{\mathrm{M}}^{\mathrm{met\ liq}}$) at a given temperature for a given metal composition were calculated using a thermodynamic approach that incorporates the interactions between the different elements

(http://norris.org.au/expet/metalact/; Wade and Wood, 2005). Interaction parameters ($\gamma_{\mathrm{M}}^{\mathrm{met\ liq}}$) describing the interaction of the various volatile elements (Cu, Zn, Ga, Ge, Se, Cd, In, Sn, Te, Pb) in the metal phase are not well or not constrained at all. We therefore assumed their activity to be unity in the metal phase, which is justified by the great similarity of $K_{\mathrm{app}}^{\mathrm{met\ liq-sil\ melt}}$ values for these elements for different metal compositions (see section 3.3 and related figures).

The doping levels of the elements considered in the Fe-rich alloys (Table S.2) are insufficient to result in a meaningful change of $\gamma_{\mathrm{Fe}}^{\mathrm{met\ liq}}$; all of the Fe activity coefficient values calculated for the experiments are equal to unity, demonstrating the absence of significant element interactions in the experimental alloys (Table 1). Similar results were found for Ni, Co and Cr.

The $\gamma_{\mathrm{MO}}^{\mathrm{sil\ melt}}$ values were taken from previous studies and/or calculated using thermodynamic models. For modeling and parameterization of equilibrium constants and metal liquid-silicate melt partition coefficients, values of $\gamma_{\mathrm{FeO}}^{\mathrm{sil\ melt}}$ = 1.7 and $\gamma_{\mathrm{NiO}}^{\mathrm{sil\ melt}}$ = 3.7 were assumed (Holzheid et al., 1997; Colson, 2017). These values are appropiate for the lunar mantle during core formation and for the experimental silicate melt compositions obtained in this study. To describe the activity of $\gamma_{\mathrm{CrO}}^{\mathrm{sil\ melt}}$, we used a thermodynamic model that describes its dependency as a function of $\gamma_{\mathrm{NiO}}^{\mathrm{sil\ melt}}$ (O'Neill and Berry, 2006). The activity of CoO was modeled as a function of $\gamma_{\mathrm{NiO}}^{\mathrm{sil\ melt}}$ given the strong correlation of these parameters ($\gamma_{\mathrm{CoO}}^{\mathrm{sil\ melt}}$ = 0.30 * $\gamma_{\mathrm{NiO}}^{\mathrm{sil\ melt}}$) (Holte et al., 2018).

Finally, the metal-silicate partitioning behavior of Se and Te is not directly dependent on fO_2 (Rose-Weston et al., 2009) and for these elements we considered metal-silicate

partition coefficient D (defined as the ratio between the concentration (in wt.%) of element *i* in the metal, relative to the concentration (in wt.%) of element *i* in the silicate melt).

3.2 The effect of temperature on the siderophile behavior of Ni, Co and Cr in lunar systems

Fig. 2 shows $K_{\mathrm{app}}^{\mathrm{met\ liq-sil\ melt}}$ values for Ni, Co, Cr as a function of temperature. Our data obtained at approximately constant pressure shows that increasing temperature greatly increases the siderophile behavior of nominally lithophile element Cr and strongly decreases the iron-loving tendencies of Ni and Co (Table 2). At 5 GPa, the pressure corresponding to the present-day lunar core-mantle boundary (Weber et al., 2011), a best fit to our new data in combination with lower temperature data for lunar melts yields the fit parameters listed in Table 2 (obtained using Eq. 2). The calculated $K_{\mathrm{app}}^{\mathrm{met\ liq-sil\ melt}}$ values and temperature terms generally agree with those derived in previous studies for non-lunar silicate melt compositions (e.g., Wade and Wood, 2005; Kegler et al., 2008; Siebert et al., 2011). Wade and Wood (2005) reported temperature terms of 3100 and 2500, without uncertainties, for Ni and Co based on free-energy calculations. Siebert et al. (2011) reported temperature terms of 2900±300 for Ni, 1900±250 for Co and –3300±500 for Cr based on multiple linear regressions. Kegler et al. (2008) reported temperature terms for Ni and Co for <5 GPa data of 4600±400 and 2000±300. Thus, in case of Co and Cr, our results (2228±156; –3810±505, respectively) are generally within error with those previously derived. The temperature term derived for Ni in this study (5379±231) is higher than previous studies. This is most likely explained by the variability in the effects of temperature on the metal-silicate partitioning behavior of Ni as a function

of pressure, as proposed by Kegler et al. (2008), and by the fact that Siebert et al. (2011) incorporated Ni data obtained under a wide range of pressures (<25 GPa). Kegler et al. (2008) found that the magnitude of temperature effects on $D_{Ni}^{met\ liq-sil\ melt}$ decreases with pressure, which results in near-negligible effects of temperature at very high pressures (>25 GPa), consistent with the much lower temperature term for Ni derived by Siebert et al. (2011). Comparing our partitioning results for Ni, Co and Cr obtained for lunar compositions with previous results obtained for terrestrial compositions at a given temperature suggests that the effects of silicate melt composition on their activities in the silicate melt are limited within the compositional range considered. For Ni, Co and Cr this observation is consistent with previous metal-silicate partitioning coefficients obtained for a large variety of melt compositions, confirming that silicate melt compositions have (near)-negligible effects on $D_{Ni,\ Co,\ Cr}^{met\ liq-sil\ melt}$ (Siebert et al., 2011; Steenstra et al., 2017a).

3.3 The effects of temperature on the distribution of volatile elements between metal liquid and silicate melt

Figure 3 shows the $D_{i}^{met\ liq-sil\ melt}$ values (Se, Te) and $K_{app}^{met\ liq-sil\ melt}$ as a function of temperature. The results show that Se and Te behave significantly less siderophile at a given pressure with increasing temperature, consistent with previous experimental observations within a smaller temperature range (Fig. 3; Rose-Weston et al., 2009). The results also show that the siderophile behavior of Cu, Sn and Ge are decreased with increasing temperature (Table 2). The temperature term obtained for Cu (2485±820) is lower than the experimental results of Mahan et al. (2018) obtained for terrestrial compositions within a wider pressure range (~4150±300). The temperature term derived

for Ge in this study (~8000±1450) is more significant than that derived by Siebert et al. (2011) (~4500±390). The increase of the siderophile behavior of Zn, Cd and Pb with temperature is consistent with previous experimental results for terrestrial compositions from of Siebert et al. (2011), Ballhaus et al. (2013) and references therein. The metal-silicate partitioning behavior of In and Ga (not shown in Fig. 3) are unaffected by changes in temperature within the studied range (Table 2), which is also consistent with previous results derived for terrestrial compositions (e.g., Siebert et al., 2011; Ballhaus et al., 2013). Overall, it is observed that the derived temperature effects are consistent with the Arrhenian behavior of elemental partitioning, with non-siderophile elements showing an increase of their siderophile behavior with increasing temperature, and vice versa.

4. DISCUSSION

4.1 Constraints on thermal regime during primordial differentiation of the Moon

First, we re-assess the thermal regime during lunar differentiation using our new experimental results. Molar metal liquid-silicate melt partition coefficients ($\mathrm{D}_{\mathrm{M}}^{*}$) for Cr, Co and Ni were modeled using Eq. 3 (e.g., Siebert et al., 2011), with the newly derived temperature dependencies:

$$\log \mathrm{D}_{\mathrm{M}}^{*} = \mathrm{a} + \mathrm{b}(1/T) - \frac{\mathrm{n}}{2}\log\left(x_{\mathrm{FeO}}^{\mathrm{sil\,melt}}/x_{\mathrm{Fe}}^{\mathrm{met\,liq}}\right) - \log\left(\gamma_{\mathrm{M}}^{\mathrm{met\,liq}}/(\gamma_{\mathrm{Fe}}^{\mathrm{met\,liq}}\right) \quad (3)$$

For $x_{\mathrm{FeO}}^{\mathrm{sil\,melt}}$ we assumed the values appropiate for the lunar silicate mantle ($x_{\mathrm{FeO}}^{\mathrm{sil\,melt}}$ = 0.08±0.02; Rai and van Westrenen, 2014, and references therein), whereas $x_{\mathrm{Fe}}^{\mathrm{met\,liq}}$ was assumed to be 0.85, consistent with a Ni abundance of $x_{\mathrm{Ni}}^{\mathrm{met\,liq}}$ of 0.15 (Steenstra et al.,

2017b). This mantle FeO - core Fe range corresponds with an overall fO_2 of lunar differentiation of –2.08±0.22 units below the iron-wüstite buffer, consistent with values derived in previous studies (e.g., Steele et al., 1992; Karner et al., 2006; Rai and van Westrenen, 2014; Steenstra et al., 2016). The activities of Fe, Ni, Co and Cr in the metallic liquids ($\gamma^{\text{met liq}}_{\text{Fe, Ni, Co, Cr}}$) as a function of core composition were again calculated using a thermodynamic approach (Wade and Wood, 2005) for each modeled temperature and assumed lunar core composition, yielding an internally consistent thermodynamic model. D^*_M values from Eq. (3) were compared with lunar core-silicate Moon partition coefficients ($D_{c/m}$)'s that would be required to explain the observed depletions of Cr, Co and Ni in the silicate Moon by core formation:

$$D_{c/m\ (i)} = \left(C_{\text{bulk Moon (i)}} - x C_{\text{bulk silicate Moon (i)}}\right) / \left(C_{\text{bulk silicate Moon (i)}}\ (1-x)\right) \quad (4)$$

where $C_{\text{bulk Moon(i)}}$ and $C_{\text{bulk silicate(i)}}$ are the concentrations of element *i* in the bulk Moon and bulk silicate Moon and x is the assumed mass fraction of the lunar mantle. The concentration of Co in the lunar mantle may be slightly lower or within error with that of BSE, reflected by the required D value of <1.52. All required D values were calculated assuming a BSE bulk Moon composition.

Fig. 4a-c shows the modeling results. For a Fe-Ni lunar core without any light elements with a mass of 1.5 to 2 wt.% of the Moon (Righter et al., 2017; Williams et al., 2014), the observed Ni, Co and Cr lunar mantle depletions can be explained by their preferential partitioning into the lunar core, but only at extreme temperatures (~3200±550 K). At the low pressure and reducing conditions inferred for lunar core formation, C and S would be the only light elements to partition into the lunar core in significant quantities. Lunar

seismic constraints have been used to argue for the presence of <6 wt.% of light elements in the lunar core (Weber et al., 2011). Geochemical evidence suggests the lunar core S content is likely <0.5 wt.% (Righter et al., 2017; Steenstra et al., 2017b). The addition of 2 wt.% S yields a similar range of core formation temperatures as those inferred for a pure Fe-Ni lunar core (~3150±550 K; Fig.4d-f). Assuming 5 wt.% of S in the lunar core also provides a satisfactory fit in terms of Ni, Co and Cr at a comparable extreme lunar core-mantle differentiation temperature of ~3100±600 K. The Ni/Co ratios of the lunar mantle can be reproduced through formation of a lunar core without S or C at slightly lower temperatures (<2900 K) than those based on the models of absolute Ni, Co and Cr abundances, whereas a lunar core with 2 or 5 wt.% S reproduces the present-day Ni/Co ratio of the lunar mantle within the range of formation temperatures derived from absolute abundances of Ni, Co and Cr (Fig. 5). Although it is unlikely from current geochemical and geophysical constraints (Day, 2018; Ding et al., 2018; Righter et al., 2017; Steenstra et al., 2017b; Steenstra et al., 2018), models with more than 5 wt.% S in the lunar core could yield lower core formation temperatures. High amounts of S in the lunar core are unlikely because of both the low S abundance in the lunar interior, as discussed in section 4.1 (Righter et al., 2017; Day, 2018; Ding et al., 2018; Steenstra et al., 2018) as well as the lack of significant loss (>10%) of S during the Moon-forming event as inferred from S isotopic systematics of lunar basalts (Wing and Farquhar, 2015).

Geochemical evidence suggests that C concentrations in the lunar core are <4.6 wt.% and could be as low as 0.4 wt.% C (Righter et al., 2017; Steenstra et al., 2017b). The addition of 5 wt.% C to the lunar core would lower the temperature at which the Ni, Co and Cr lunar mantle depletions can be simultaneously satisfied to 2600±600 K. However,

the actual concentration of C in the lunar core is likely to be much lower than 5 wt.% given the potential loss of C during the Moon-forming event and the outcome of the geochemical and geophysical studies performed by Righter et al. (2017).

Finally, it should be noted that Cr is not the limiting element in any of the models described here. Any loss of Cr during the Moon-forming event or subsequent lunar differentiation (Sossi et al., 2018) would therefore not affect the geochemical models described above.

4.2 Uncertainties related to estimating the thermal state of lunar differentiation by Ni/Co

Segregation of metal- and/or sulfide liquids from the lunar mantle at any stage after lunar core formation could have affected the abundance and ratios of Ni and Co. However, significant quantities of residual sulfides in low-Ti basalts and glasses source regions are excluded by both low S abundances and elemental correlations of Ni, Co and Cu (Day, 2018; Ding et al., 2018; Steenstra et al., 2018), as it has been shown that these elements behave only mildly compatible (Ni, Co) to mildly incompatible (Cu) in primitive lunar low-Ti magmatic samples. Although Wänke et al. (2018) and Brenan et al. (2019) showed that some of the low-Ti melts could have experienced saturation of a S-poor sulfide during some stages of their magmatic evolution, Brenan et al. (2019) concluded that the modal abundances of these phases were sufficiently low (approx. 10 ppm) to have no measurable effect on the abundances of moderately siderophile elements such as Ni and Co (Brenan et al., 2019). On the other hand, Xia et al. (2019) recently argued for significant sulfide fractionation during lunar differentiation, based on the Cu isotope

composition of the silicate Moon. However, their model relies solely on the assumption of 3500–7500 ppm S in the bulk Moon (i.e., enrichment of bulk Moon to BSE by a factor of 13–27 in terms of S), which is inconsistent with current of lunar formation, bulk Moon compositions and geophysical properties of the lunar core (e.g., Steenstra et al., 2017b and references therein). We therefore conclude that the derived temperature range for the initial Moon is unlikely to be affected by potential metal- or sulfide saturation in the low-Ti basalt source regions.

It should also be assessed whether a shallow LMO and/or partial lunar core-silicate melt equilibration could instead yield the Ni and Co abundances in the lunar interior. Due to the negative effects of pressure on Ni and Co partitioning (Kegler et al., 2008; Siebert et al., 2011), lower pressure shallow- or intermediate depth LMO scenarios (e.g., Charlier et al., 2018) would increase the discrepancies between modeled and observed depletions even further. Partial equilibration of the lunar core with the lunar mantle could result in less strong mantle depletions of Ni and Co during core-mantle differentiation, but this would be at odds with the measured lunar mantle HSE depletions and the proposed replenishment of these elements during a late veneer on the Moon (Day et al., 2007; Kruijer et al., 2015). Significant disequilibrium between lunar core and mantle would likely be reflected by proto-BSE (i.e., non-chondritic) signatures of HSE in lunar materials, especially at the extent that is required to significantly disturb Co and Ni abundances in the lunar mantle. A large degree of bulk silicate Moon homogenization is also consistent with the identical Sm-Nd isotopic equilibria observed in lunar samples derived from distinctly different regions of the lunar interior (Borg et al., 2019).

The sensitivity of the outcome of our models to the effect of a late veneer should also be assessed. The abundances of Ni and Co in the BSE and lunar mantle could have been affected by the addition of chondritic late veneers of a 0.3 to 0.7 mass % (Bottke et al., 2010; Wang and Becker, 2015) to the Earth and 0.02 to 0.05 mass % (Kruijer et al., 2015) to the Moon. In case of the bulk silicate Earth, such a late veneer would increase pre-late veneer BSE Ni contents by 30 to 125 ppm and Co abundances by 1.5–6 ppm, the exact amount depending on the composition of chondritic late veneer impactors (Newsom, 1995). Stripping out these amounts of Ni and Co from the (present-day) BSE values used to model the composition of the bulk Moon, the metal-silicate partition coefficients required to explain their depletions in the lunar mantle are even lower, implying higher lunar core formation temperatures. For the Moon, a late veneer contribution corresponds to the addition of approximately 2 to 9 ppm Ni and less than 0.5 ppm Co. The maximum proposed extents of late veneers based on HSE abundances and W isotopes therefore do not significantly alter the abundances of Ni and Co in the BSM. The high-temperature differentiation of the Moon suggested by our calculations is therefore not affected by assumptions about late veneer additions to Earth and Moon.

Finally, uncertainties in the actual fO_2 during lunar core formation could affect the modeled temperature range. In the above calculations a fO_2 of $\Delta IW = -2.08 \pm 0.22$ is assumed, based on the assumption that the FeO content of the bulk Moon is identical to that of the present-day bulk silicate Earth, as implied from Fe isotopes (Sossi and Moynier, 2017) as well as the overall geochemical similarity of the bulk silicate Earth and the bulk Moon (e.g., Zhang et al., 2012; Kruijer et al., 2015; Young et al., 2016). It should be noted that current density models of the lunar interior do permit a slight enrichment of

the bulk Moon compared to the present-day BSE (Dauphas et a., 2014), although the corresponding uncertainties are significant. In this case, the modeled fO_2 would be closer to ΔIW = –1.5 or at maximum –1, thereby decreasing the modeled temperature range due to less siderophile behavior of Ni and Co at such conditions. However, we again emphasize that current geochemical evidence is not consistent with an FeO enrichment of the bulk Moon compared to BSE.

4.3 Lunar core formation at high temperatures

High-temperature lunar core formation (at temperatures of >2600 to up to 3700 K, depending on the assumed light element content of the core) is thus the most plausible process to explain the observed lunar mantle depletions of Ni and Co. This temperature estimate is a lower limit as it reflects the last recorded stage of metal-silicate equilibrium during lunar differentiation. In this scenario, it is assumed that the super-liquidus Ni and Co signature of the lunar mantle was preserved due to rapid cooling of the lunar mantle and core, relative to the timescales of convective mixing within the lunar interior, following core formation. It should be noted that rapid crystallization of the lunar magma ocean is also reflected by Sm-Nd systematics of primitive lunar samples (Borg et al., 2019).The only feasible mechanism to obtain such high temperatures during initial lunar differentiation is through a high-energy giant impact. The proposed temperatures are compatible with the evolution of BSE compositional vapors at pressures exceeding >20 bar, where the majority of lunar mass (> 80 per cent) has re-accreted to form the Moon (Lock et al., 2018). High-temperature differentiation of the Moon is also consistent with the existence of a deep, global lunar magma ocean inferred for the early Moon from

pristine volcanic glasses (Longhi, 2006) and with the extensive volatile loss during the early evolution of the Moon, relative to other terrestrial bodies (Wang and Jacobsen, 2016; Kato and Moynier, 2017) (see also next section). Finally, it also reproduces the required Hf/W of the silicate Moon (Thiemens et al., 2019) (see Appendix section A.5).

4.4 Siderophile behavior of volatile elements during a high-temperature Moon forming event?

In light of lunar core formation temperatures based on Ni and Co data, we assess to what extent volatile elements Cu, Zn, Ga, Ge, Se, Cd, In, Sn, Te, Pb could have partitioned into the lunar core during high temperature differentiation of the Moon. Modeling results for a Fe-Ni lunar core (Fig. 6) show that at temperatures lower than ~2500–2700 K, the lunar mantle depletions of Se, Cu, Te, Ge and Sn can be largely if not fully reconciled with core formation only, generally consistent with our previous results (Steenstra et al., 2016, 2017c) (summarized in Fig. 7).This is extended to ~3200 K for Sn (Fig. 6). At higher temperatures, increasingly more volatility-related loss of these elements is required for explain their present-day abundances in the lunar mantle (Fig. 7). Due to the positive effect of temperature on the siderophile behavior of Zn, Cd and Pb, required volatility-related loss slightly decreases with increasing core formation temperatures. However, it is clear that no lunar core formation scenario can fully explain the depletions of the latter elements and that significant volatility-related loss is required. These results are consistent with the work of Righter (2019) and with the Zn isotopic composition of the silicate Moon (e.g., Paniello et al., 2012; Day et al., 2019).

Figure 7 also shows that high-temperature core formation in the Moon may be a viable mechanism to explain the apparent ‘’overabundance’’ of some of these elements (Cu, Ge, Se, Te, Sn) in the silicate Moon, compared to other elements of similar volatility (Wolf and Anders, 1980; Hauri et al., 2015). It has been shown that at intermediate temperatures of metal-silicate equilibration (~2200 K, Steenstra et al., 2016; 2017c), virtually no volatility-related loss of the latter elements is required, as also indicated in Fig. 7. Indeed, volatility-related loss of both Cu and Sn during the formation and/or differentiation of the Moon is strongly indicated from the light Sn and heavy Cu isotopic compositions of lunar materials (Herzog et al., 2009; Wang et al., 2019). Lunar core formation at super-liquidus temperatures may therefore be more consistent with observed silicate Moon depletions of Cu, Se, Sn and Te, especially in light of recent results for other similarly volatile elements (e.g., Day et al., 2019).

On the other hand, it has also been suggested that the abundances of the more volatile siderophile- and chalcophile elements Ag, Bi, Cd, In, Sb, Sn, Tl and Zn and their CI chondritic-like proportions reflect a thin veneer of ordinary or CI-chondrite-like material to the Moon (Wolf and Anders, 1980, O’Neill, 1991). However, in light of current geochemical constraints on delivered late veneer mass (e.g., 0.02 to 0.05 mass %; Kruijer et al., 2015), it is deemed unlikely that the abundances of the majority of the elements of interest in the lunar mantle would be significantly affected by a late veneer (Table S.3), especially given their volatile nature and expected degassing upon impact.

5. CONCLUSIONS

The dependence of the metal liquid-silicate melt partitioning of Ni, Co, Cr and various volatile trace elements (Cu, Zn, Ga, Ge, Se, Cd, In, Sn, Te, Pb) on temperature was experimentally constrained at lunar-relevant pressures. The depletions of Ni and Co in the lunar mantle, in conjunction their metal-silicate partitioning behavior at high temperatures, indicate that studies of the thermal history of the Moon should start with a superheated fully molten body. They also suggest that the geochemical composition of the lunar mantle provides quantitative boundary conditions for the thermal state of the Moon that can validate numerical models of Moon formation. Our experimental results show that lunar core formation at high (>2650 K) temperatures, as inferred from Ni and Co systematics, would require significantly (more) volatility-related loss of Cu, Ge, Sn and most notably Se and Te, as their siderophile behavior would be significantly decreased, compared to moderate lunar core formation temperatures (~2200 K). Core formation at super-liquidus temperatures would result in slightly less required volatility-related loss of Pb, Cd, whereas the abundances of Zn, In and Ga in the silicate Moon are virtually unaffected by core formation, even at high temperatures.

Acknowledgements

We would like to thank M. Duncan for her assistance in the experiments presented in this study. This work was supported by a Netherlands Organization for Scientific Research (N.W.O.) Vici award to W.v.W., a Carnegie Postdoctoral Fellowship to E.S.S. Experiments were also supported by NASA grant to Y.F. (NNX17AE30G) and by the DFG

(German Research Foundation) – Project-D 263649064 – SFB TRR-170 publication no. 93. We thank John Brodholt for editorial handling and thorough reviews by P. Sossi and an anonymous reviewer that significantly improved the quality of the manuscript.

REFERENCES

Ballhaus C., Laurenz V., Münker C., Fonseca R.O.C., Albarède F., Rohrbach A., Lagos M., Schmidt M.W., Jochum K.-P., Stoll G., Weis U., Helmy H.M. (2013) The U/Pb ratio of the Earth's mantle - a signature of late volatile addition. *Earth Planet. Sci. Lett.* **362**, 237–245.

Benz W., Slattery W.L., Cameron a.G.W. (1986) The origin of the moon and the single-impact hypothesis I. *Icarus* **66,** 515–535.

Borg L.E., Gaffney A.M., Kruijer T.S., Marks N.A., Sio C.K., Wimpenny J. (2019) Isotopic evidence for a young lunar magma ocean. *Earth Planet. Sci. Lett.* **523,** 115706.

Bottke W. F., Walker R. J., Day J. M. D., Nesvorny D., Elkins-Tanton L. (2010) Stochastic late accretion to Earth, the Moon, and Mars. *Science* **330**, 1527–1530.

Brenan J. M., Mungall J. E., Bennet N. R. (2019) Abundance of highly siderophile elements in lunar basalts controlled by iron sulfide melts. *Nat. Geosci.* **12**, 701–706.

Cameron A.G.W., Ward W.R. (1976) The origin of the Moon. *Lunar Sci. VII,* 120–122.

Canup R.M. (2012) Forming a moon with an Earth-like composition via a giant impact. *Science* **338**, 1052–1055.

Chabot N.L., Agee C.B. (2003) Core formation in the Earth and Moon: New experimental constraints from V, Cr, and Mn. *Geochim. Cosmochim. Acta* **67**, 2077–2091.

Charlier B., Grove T.L., Namur O., Holtz F. (2018) Crystallization of the lunar magma

ocean and the primordial mantle-crust differentiation of the Moon. *Geochim. Cosmochim. Acta* **234**, 50–69.

Charnoz S., Michaut C. (2015) Evolution of the protolunar disk: Dynamics, cooling timescale and implantation of volatiles onto the Earth. *Icarus* **260,** 440–463.

Colson R.O. (2017) An approach to modeling trace component activities in silicate melts: NiO. *Contrib. to Mineral. Petrol.* **172**, doi:10.1007/s00410-017-1361-1.

Ćuk M., Hamilton D. P., Lock S. J., Stewart S. T. (2016) Tidal evolution of the Moon from a high-obliquity, high-angular-momentum Earth. *Nature* **539**, 402–406.

Dauphas N., Burkhardt C., Warren P.H., Teng F.Z. (2014) Geochemical arguments for an Earth-like Moon-forming impactor. *PTRAS* **372** doi:10.1098/rsta.2013.0244.

Day J. M. D. (2018) Geochemical constraints on residual metal and sulfide in the sources of lunar mare basalts. *Am. Mineral.* **103**, 1734–1740.

Day J. M. D., Pearson D. G., Taylor L. A. (2007) Highly Siderophile Element Constraints on Accretion and Differentiation of the Earth-Moon System. *Science* **315**, 217–219.

Day J. M. D., van Kooten E. M. M. E., Hofmann B. A., Moynier F. (2019) Mare basalt meteorites, magnesian-suite rocks and KREEP reveal loss of zinc during and after lunar formation. *Earth Planet. Sci. Lett.* doi.org/10.1016/j.epsl.2019.115998.

Delano J.W. (1986). In: *Origin of the Moon*, pp. 231–248.

Hauri E. H., Saal A. E., Rutherford M. J., Van Orman J. A. (2015) Water in the moon's interior: Truth and consequences. *Earth Planet. Sci. Lett.* **409**, 252–264.

Herzog G. F., Moynier F., Albarede F., Berezhnoy A. A. (2009) Isotopic and elemental abundances of copper and zinc in lunar samples, Zagami, Pele's hairs, and a terrestrial basalts.

Holte E.P., Dougherty E.B., Colson R.O. (2018) Experimental Measurements of CoO Activities in Silicate Melts. *LPSC* **49th** #1479 (abstr.)

Holzheid A., Palme H., Chakraborty S. (1997) The activities of NiO, CoO and FeO in silicate melts. *Chem. Geol.* **139**, 21–38.

Jones J.H., Palme H. (2000) in *Origin of the Earth and Moon*, pp. 197–216.

Karner J.M., Sutton S.R., Papike J.J., Shearer C.K., Jones J.H. and Newville M. (2006) Application of a new vanadium valence oxybarometer to basaltic glasses from the Earth, Moon, and Mars. *Am. Mineral.* **91,** 270–277.

Kato C., Moynier F. (2017) Gallium isotopic evidence for extensive volatile loss from the Moon during its formation. *Sci. Adv.* **3**, e1700571.

Kegler P., Holzheid D.J., Frost D., Rubie D.C., Dohmen R., Palme H. (2008). New Ni and Co metal-silicate partitioning data and their relevance for an early terrestrial magma ocean. *Earth Planet. Sci. Lett.* **268**, 28–40.

Kruijer T.S., Kleine T., Fischer-Gödde M., Sprung P. (2015) Lunar tungsten isotopic evidence for the late veneer. *Nature* **520**, 534–537.

Lock S. J., Stewart S. T., Petaev M. I., Leinhardt Z., Mace M. T., Jacobsen S. B., Cuk M. (2018) The Origin of the Moon Within a Terrestrial Synestia. *J. Geophys. Res. Planets*. **123**, 910–951.

Lin Y., Tronche E.J., Steenstra E.S., van Westrenen W. (2016) Evidence for an early wet Moon from experimental crystallization of the lunar magma ocean. *Nat. Geosci.* **10**, 14–18.

Longhi J. (2006) Petrogenesis of picritic mare magmas: Constraints on the extent of early lunar differentiation. *Geochim. Cosmochim. Acta* **70**, 5919–5934.

Newsom H.E. (1995) Composition of the Solar System, Planets, Meteorites, and Major Terrestrial Reservoirs. *Glob. Earth Phys.*, doi:doi:10.1029/RF001p0159.

Ni P., Zhang Y., Chen S., Gagnon J. (2019) A melt inclusion study on volatile abundances in the lunar mantle. *Geochim. Cosmochim. Acta* **249,** 17–41.

Norris C.A., Wood B.J. (2017) Earth's volatile contents established by melting and vaporization. *Nature* **549**, 507–510.

O'Neill H. S. C. (1991) The origin of the moon and the early history of the earth - A chemical model. Part 1: The moon. *Geochim. Cosmochim. Acta* **55**, 1135–1157.

O'Neill H. S. C., Berry A. J. (2006) Activity coefficients at low dilution of CrO, NiO and CoO in melts in the system CaO-MgO-Al_2O_3-SiO_2 at 1400°C: Using the thermodynamic behaviour of transition metal oxides in silicate melts to probe their structure. *Chem. Geol.* **231**, 77–89.

Paniello R.C., Day J.M.D., Moynier F. (2012) Zinc isotopic evidence for the origin of the Moon. *Nature* **490**, 376–379.

Pringle E.A., Moynier F. (2017) Rubidium isotopic composition of the Earth, meteorites, and the Moon: Evidence for the origin of volatile loss during planetary accretion. *Earth Planet. Sci. Lett.* **473**, 62–70.

Righter K., Go B.M., Pando K.A., Danielson L., Ross D.K., Zahman Z., Keller L.P. (2017). Phase equilibria of a low S and C lunar core: Implications for an early lunar dynamo and physical state of the current core. *Earth Planet. Sci. Lett.* **463**, 323–332.

Righter K. (2019) Volatile element depletion of the Moon – The roles of precursors, post-impact dynamics, and core formation. *Sci. Adv.* **5,** eaau7658.

Rose-Weston L., Brenan J.M., Fei Y., Secco R.A., Frost D.J. (2009) Effect of pressure,

temperature, and oxygen fugacity on the metal-silicate partitioning of Te, Se, and S: Implications for earth differentiation. *Geochim. Cosmochim. Act.* **73**, 4598–4615.

Rufu R., Aharonson O., Perets H. (2017) A multiple-impact origin for the Moon. *Nat. Geosci.* **10,** 89–94.

Siebert J., Corgne A., Ryerson F.J. (2011) Systematics of metal-silicate partitioning for many siderophile elements applied to Earth's core formation. *Geochim. Cosmochim. Acta*. **75**, 1451–1489.

Sossi P.A., Moynier F., van Zuilen K. (2018) Volatile loss following cooling and accretion of the Moon revealed by chromium isotopes. *PNAS* 201809060.

Sossi P.A., Moynier F. (2017) Chemical and isotopic kinship of iron in the Earth and Moon deduced from the lunar Mg-Suite. *Earth Planet. Sci. Lett.* **471**, 125–135.

Steele A.M., Colson R.O., Kortev R.L., Haskin L.A. (1992) Apollo1 5 green glass: Compositional distribution and petrogenesis. *Geochim. Cosmochim. Acta* **56,** 2253–2265.

Steenstra E.S., Rai N., Knibbe J.S., Lin Y.H., van Westrenen W. (2016) New geochemical models of core formation in the Moon from metal-silicate partitioning of 15 siderophile elements. *Earth Planet. Sci. Lett.* **441**, 1–9.

Steenstra E.S., Sitabi A.B., Lin Y.H., Rai N., Knibbe J.S., Berndt J., Matveev S., van Westrenen, W. (2017a) The effect of melt composition on metal-silicate partitioning of siderophile elements and constraints on core formation in the angrite parent body. *Geochim. Cosmochim. Acta*. **212,** 62–83.

Steenstra E.S., Lin Y.H., Rai N., Jansen M., van Westrenen W. (2017b) Carbon as the dominant light element in the lunar core. *Am. Mineral.* **102**, 92–97.

Steenstra E.S., Lin Y.H., Dankers D., Rai N., Berndt J., Matveev S., van Westrenen W. (2017c) The lunar core can be a major reservoir for volatile elements S, Se, Te and Sb. Sci. Rep. **7**, 14552.

Steenstra E.S., Seegers A.X., Eising J., Tomassen B. G. J., Webers F. P. F., Berndt J., Klemme S., Matveev S., van Westrenen W. (2018) Evidence for a sulfur-undersaturated lunar interior from the solubility of sulfur in lunar melts and sulfide-silicate partitioning of siderophile elements. *Geochim. Cosmochim. Acta*. **231**, 130–156.

Steenstra E.S., Berndt J., Klemme S., van Westrenen W. (2019) LA-ICP-MS analyses of Fe-rich alloys: quantification of matrix effects for 193 nm excimer laser systems. *J. Analytical Atom. Spectrometr.* **34**, 222–231.

Terasaki H., Frost D. J., Rubie D. C., Langenhorst F. (2008) Percolative core formation in planetesimals. *Earth Planet. Sci. Lett.* **273**, 132–137.

Thibault Y., Walter M. J. (1995) The influence of pressure and temperature on the metal-silicate partition coefficients of nickel and cobalt in a model C1 chondrite and implications for metal segregation in a deep magma ocean. *Geochim. Cosmochim. Acta* **59**, 991–1002.

Thiemens M.W., Sprung P., Fonseca R.O.C., Leitzke F.P., Munker C. (2019) Early Moon formation inferred from hafnium-tungsten systematics. *Nat. Geosci.,* doi:10.1038/s41561-019-0398-3.

Wade J., Wood B.J. (2005) Core formation and the oxidation state of the Earth. *Earth Planet. Sci. Lett.* **236**, 78–95.

Wang K., Jacobsen S.B. (2016) Potassium isotopic evidence for a high-energy giant

impact origin of the Moon. *Nature* **538**, 487–490.

Wang Z., Becker H. (2013) Ratios of S, Se and Te in the silicate Earth require a volatile-rich late veneer. *Nature* **499**, 328–331.

Wang H.S., Lineweaver C.H., Ireland T.R. (2018) The elemental abundances (with uncertainties) of the most Earth-like planet. *Icarus* **299**, 460–474.

Wang X., Fitoussi C., Bourdon B., Fegley Jr B., Charnoz S. (2019) Tin isotopes indicative of liquid-vapor equilibration and separation in the Moon-forming disk. *Nat. Geosci.* **12,** 707–711.

Wanke H., Dreibus G., Palme H. (1978) Primary matter in the lunar highlands: the case of the siderophile elements. *9th Proceed. Lunar Planet. Sci. Conf.* 83–110.

Williams J. G. *et al.* (2014) Lunar interior properties from the GRAIL mission. *J. Geophys. Res. Planets* **119**, 1546–1578.

Weber R.C., Lin P.-Y., Garnero E. J., Williams Q., Lognonne P. (2011) Seismic Detection of the Lunar Core. *Science* **331**, 309–312.

Wing B. A., Farquhar J. (2015) Sulfur isotope homogeneity of lunar mare basalts. *Geochim. Cosmochim. Acta* **170**, 266–280.

Wolf R., Anders E. (1980) Moon and Earth: compositional differences inferred from siderophiles, volatiles, and alkalis in basalts. *Geochim. Cosmochim. Acta* **44,** 2111–2124.

Young E.D., Kohl I.E., Warren P.H., Rubie R.C., Jacobson S.A., Morbidelli A. (2016) Oxygen isotopic evidence for vigorous mixing during the Moon-forming giant impact. *Science* **351**, 493–496.

Zhang J., Dauphas N., Davis A.M., Leya I, Fedkin A. (2012) The proto-Earth as a

significant source of lunar material. *Nat. Geosci.* **5**, 251–255.

Figure captions

Fig. 1. Backscattered electron images of run products PR1518, PR1521 and PR1539. Analytical spots from LA-ICP-MS analyses are visible in both metal and silicate phases.

Fig. 2. The $\mathrm{K}_{\mathrm{app}}^{\mathrm{met\ liq-sil\ melt}}$ values of Ni, Co and Cr as a function of temperature from this study and previous studies. Exchange coefficients were normalized to 5 GPa using the pressure terms from a previous study (Siebert et al., 2011). High-temperature data (circles) from this study. Lower temperature data using similar capsules, lunar compositions and analytical tools were taken from Steenstra et al. (2017a, c). Errors are maximum errors calculated using simple error propagation while assuming 2 SE on EPMA and LA-ICP-MS concentrations.

Fig. 3. The $\mathrm{K}_{\mathrm{app}}^{\mathrm{met\ liq-sil\ melt}}$ and $\mathrm{D}_{\mathrm{i}}^{\mathrm{met\ liq-sil\ melt}}$ values of various volatile elements for lunar compositions as a function of temperature from this study and a previous study (Steenstra et al., 2017c). Errors are maximum errors calculated using simple error propagation while assuming 2 SE on EPMA and LA-ICP-MS concentrations.

Fig. 4. Modeled $\mathrm{D}_{\mathrm{Ni,\ Co,\ Cr}}^{\mathrm{met\ liq-sil\ melt}}$ values at 5 GPa as a function of temperature for **(a-c)** a 1.5 to 2 mass% Fe-Ni lunar core and **(d-f)** 1.5 to 2 mass%, 2 wt.% S bearing Fe-Ni lunar core. Horizontal bars represent the values required to explain their depletions in the lunar

mantle by core formation (Table 2). Modeled D range includes uncertainties in fitting terms (see Table 2).

Fig. 5. Modeled Ni/Co ratios as a result of lunar core formation versus temperature for a 1.5–2 mass% Fe-Ni lunar core with 2 wt.% S.

Fig. 6. Modeled $\mathrm{D}_{\mathrm{i}}^{\mathrm{met\ liq-sil\ melt}}$ values for various volatile elements (obtained at ~3.8 GPa, normalized in case of Se and Te to 5 GPa) as a function of temperature for a 1.5 to 2 mass% Fe-Ni lunar core. Horizontal bars represent the values required to explain their depletions in the lunar mantle by core formation; modeled D range includes uncertainties in fitting terms (see Table 2).

Fig 7. Modeled and measured elemental abundances of volatile (siderophile /chalcophile) elements in the lunar mantle (in ppm) expressed as absolute concentrations (upper panel) or normalized to bulk silicate Earth (lower panel). Elemental abundances were modeled assuming (1) no core formation depletion (as indicated by triangles and grey solid line), (2) by consideration of lunar core formation at –2.10±0.2 units below the iron-wüstite buffer and 2200 K, corresponding to the approximate liquidus temperature at the lunar core/mantle boundary (Rai and van Westrenen, 2014) (as indicated by blue squares and the dine dashed line) and (3) by considering lunar differentiation at super-liquidus temperatures (3500 K), as indicated by red squares and by the coarse dashed line. Measured elemental abundances (green circles and corresponding fine-dashed line) were taken from Hauri et al. (2015) and references therein (see Table 2). Previous bulk

silicate Moon estimates from O'Neill (1991) and Ni et al. (2019), as indicated by light green diamonds and triangles, are plotted for comparison purposes.

Table 1 Experimental run conditions and measured metal-silicate partition coefficients. Numbers in brackets are errors in terms of least digits cited and calculated through simple error propagation while assuming 2 SE on EPMA and LA-ICP-MS analyses.

Run #	*P* (GPa)	*T* (K)	time (s)	Comp.[a]	ΔIW [b]	D [c] Ni	Co	Cr	Cu	Zn	Ga	Ge	Se	Cd	In	Sn	Sb	Te	Pb
PR1446	3.3	2173	300	GG; A	–1.94	1193(65)	–	–	–	–	–	–	–	–	–	–	–	–	–
PR1449	3.9	2123[c]	300	GG; A	–2.49	2105(118)	–	1.08(14)	29(4)	1.37(8)	1.41(24)	–	27(5)	2.2(5)	8.3(15)	43(9)	5976(1612)	108(20)	8.6(22)
PR1450	3.8	2373	240	GG; A	–2.44	734(143)	–	1.09(19)	14.6(40)	1.64(16)	1.47(24)	–	13.4(55)	4.1(11)	8.4(38)	28(9)	1349(640)	15.2(58)	11.6(38)
PR1465	3.8	2460[c]	180	GG; A	–2.47	1437(464)	–	1.06(42)	25(4)	1.17(8)	1.26(57)	–	11.1(50)	2.0(7)	12.1(43)	>12.2(8)	4241(3860)	14.3(67)	8.7(25)
PR1468	3.8	2073	120	GG; A	–1.82	1322(52)	–	–	5.5(16)	1.24(63)	–	–	28(7)	0.46(20)	8.5(11)	72(42)	25655(3116)	52(11)	1.42(51)
PR1470	3.8	2473	60	GG; B	–2.01	400(34)	174(9)	0.51(3)	14.6(19)	1.86(25)	2.66(56)	686(56)	–	–	–	35(13)	–	–	20(5)
PR1477	3.8	2273	120	GG; A	–2.19	795(59)	–	0.21(6)	32(10)	1.74(20)	2.83(83)	–	36(10)	3.0(8)	15.9(41)	22(6)	954(223)	79(20)	11.6(30)
PR1480	3.8	2473	60	GG; A	–2.19	558(132)	–	0.32(13)	25(9)	2.99(41)	6.2(18)	–	7.3(23)	5.5(23)	15.8(53)	>49(21)	910(313)	1.91(68)	25(14)
PR1481	3.8	2373	90	GG; B	–2.27	670(154)	283(35)	0.49(5)	–	–	–	750(354)	–	–	–	–	–	–	–
PR1489	3.8	2573[c]	75	GG; A	–2.42	678(115)	–	1.23(31)	18.4(47)	3.93(58)	3.11(85)	–	5.0(35)	7.1(25)	b.d.l.	>40(13)	4018(1415)	19(6)	24(10)
PR1491	3.8	2673[c]	90	GG; A	–2.49	521(93)	–	0.50(10)	13.9(30)	1.66(15)	3.30(76)	–	1.80(82)	1.38(43)	13.8(44)	14(4)	6883(2380)	2.50(85)	9.7(34)
PR1505	3.8	2673[c]	40	GG; B	–2.08	6450(695)	185(10)	0.57(4)	17.6(52)	1.13(20)	2.18(45)	566(72)	–	–	–	10.6(14)	–	–	13.8(23)
PR1506	3.8	2573[c]	60	GG; B	–2.09	4900(523)	156(6)	0.38(7)	12.1(19)	1.14(24)	2.54(59)	318(33)	–	–	–	8.5(12)	–	–	10.7(34)
PR1508	3.8	2773[c]	40	GG; A	–2.43	421(82)	–	1.64(16)	21(8)	3.83(35)	3.20(70)	–	4.8(13)	5.1(23)	19.1(54)	>42(11)	929(368)	5.0(19)	17.4(108)
PR1510	3.8	2773[c]	40	GG; B	–2.12	176(10)	113(6)	1.57(10)	9.9(22)	0.94(36)	b.d.l.	127(11)	–	–	–	10.9(31)	–	–	b.d.l.
PR1517	3.8	2773[c]	30	GG; B	–1.91	177(23)	111(14)	1.78(34)	15.1(28)	2.33(51)	4.57(94)	294(47)	–	–	–	–	–	–	15.8(47)
PR1518	3.8	2873[c]	30	GG; B	–2.05	201(13)	111(5)	0.70(6)	11.9(12)	1.36(19)	4.72(70)	386(27)	–	–	–	–	–	–	15.3(38)
PR1521	3.8	2873[c]	30	GG; B	–2.09	134(11)	84(7)	1.42(18)	10.2(22)	2.89(64)	5.15(32)	293(24)	–	–	–	–	–	–	23(5)
PR1522	3.2	2473	120	GG; A	–2.29	1141(133)	–	0.54(14)	21(5)	2.65(27)	3.49(34)	–	8.8(23)	3.8(15)	36(7)	47(7)	14309(5850)	19.0(43)	22(14)
PR1524	3.8	2773[c]	30	GG; A	–2.04	243(80)	–	0.64(14)	9.6(23)	3.42(27)	3.64(92)	–	2.51(106)	2.1(10)	15.7(66)	b.d.l.	1005(375)	2.94(123)	8.5(4.5)
PR1538	3.8	1973	600	GG; B	–1.51	1158(113)	241(13)	0.18(2)	6.3(12)	0.35(5)	1.52(26)	3175(368)	–	–	–	6.0(22)	–	–	2.7(7)
PR1539	3.2	2473	90	GG; B	–2.02	424(29)	181(11)	0.61(6)	22(7)	2.40(35)	b.d.l.	716(48)	–	–	–	–	–	–	28(5)
PR1561	3.8	2173	660	GG; A	–1.63	1800(62)	–	0.24(2)	46(6)	0.49(3)	1.55(24)	–	83(13)	0.88(15)	15.6(23)	34(9)	38921(9683)	311(63)	5.4(11)

[a] GG = lunar Apollo 15 green glass; A and B denote the type of metal composition used in the experiments (A = Fe + 1 wt.% Si, 5 wt.% Ni, 1.5 wt.% As, Se, Cd, In, Sb, Te, Pb; B = Fe + 1.5 wt.% P, V, Cr, Mn, Co, Ni, Ge, Mo, W) [b] Calculated assuming $\gamma_{\mathrm{FeO}}^{\mathrm{sil\ melt}}$ = 1.7 [c] Temperature was estimated using power-*T* relationships derived with thermocouple at the same pressures and assembly; uncertainties are estimated to be ±50 K. [c] Measured metal-silicate partition coefficient D, defined here as the defined as the wt% ratio of element i in the metal liquid and silicate melt, respectively.

Table 2 Fitting results and abundances of the elements considered in the bulk silicate Earth (BSE) and in the bulk silicate Moon (BSM) and corresponding log D values (calculated using Eq. 4) required to explain their lunar mantle depletions for a 1.5 to 2 mass% lunar core. The log Kapp values (Ni, Co) and log D values (Se, Te) were prior to regressions normalized to a common pressure of 5 GPa, respectively, using the pressure and/or FeO dependencies from Siebert et al. (2011) and Steenstra et al. (2017c), respectively.

	A	**B(1/T)**	***N***	***R²*** [a]	**bulk Moon abundance**	**bulk silicate Moon** [b]	**required log D core/mantle** [c]
Cr^{2+}	0.51(24)	–3810(505)	31	0.61	2580±190 (ppm)[1]	2050±150 (ppm)[2-4]	0.87±0.62
Co^{2+}	0.10(8)	2228(156)	17	0.91	103±4[1]	90±18[b3,4]	<1.52
Ni^{2+}	–1.16(11)	5379(231)	31	0.93	1900±80[1]	505±85[3,4]	2.21±0.18
Cu^{1+}	0.17(32)	2564(819)	18	0.38	28±4[1]	7.2±1.4[3]	2.26±0.04
Zn^{2+}	0.37(40)	–2873(988)	21	0.30	54±3[1]	7.7±1.5[3]	2.59±0.33
Ga^{3+} [d]	–	–	–	–	4.3±0.2[1]	2.3±0.5[3]	1.74±0.44
Cd^{2+}	1.45(73)	–4438(1759)	12	0.39	38±6 (ppb)[1]	12±2.4 (ppb)[3]	2.12±0.43
In^{3+} [d]	–	–	–	–	13±2[1]	1.66±0.69[3]	2.65±0.37
Sn^{2+}	–1.42(71)	4498(1696)	20	0.44	118±19[1]	39±8[3]	2.10±0.44
Ge^{2+}	–1.38(56)	8040(1433)	9	0.82	1140±120[1]	15±3[3]	3.68±0.33
Pb^{2+}	1.47(39)	–3370(957)	19	0.42	167±14[1]	28±6[3]	2.51±0.35
Se	–3.23(29)	10982(583)	36	0.91	80±17[5]	24±5[3]	2.17±0.41
Te	–2.95(37)	10891(725)	36	0.87	11±1.7[5]	4.1±0.8[3]	2.04±0.40

References: [1] Wang et al. (2018) [2] Sossi et al. (2018) [3] Hauri et al. (2015) [4] Delano (1986) [5] Wang and Becker (2013) [a] Low R^2 reflects an absence of temperature effects (i.e., the variability of elemental metal-silicate partitioning is predominantly explained by variability in fO_2) and is not indicative of overall scatter of D values [b] Assuming a 20 % uncertainty on lunar mantle estimates of Co, Cu, Zn, Cd, In, Sn, Ge, Ga, Pb, Se, Te as no uncertainties were reported in Hauri et al. (2015) [c] Calculated using Eq. (4) [d] The siderophile behavior of In and Ga is unaffected by temperature within the studied range – for modelling we therefore assumed $D_{Ga}^{met\ liq-sil\ melt}$ = 3 and $D_{In}^{met\ liq-sil\ melt}$ = 10 (Table 1).

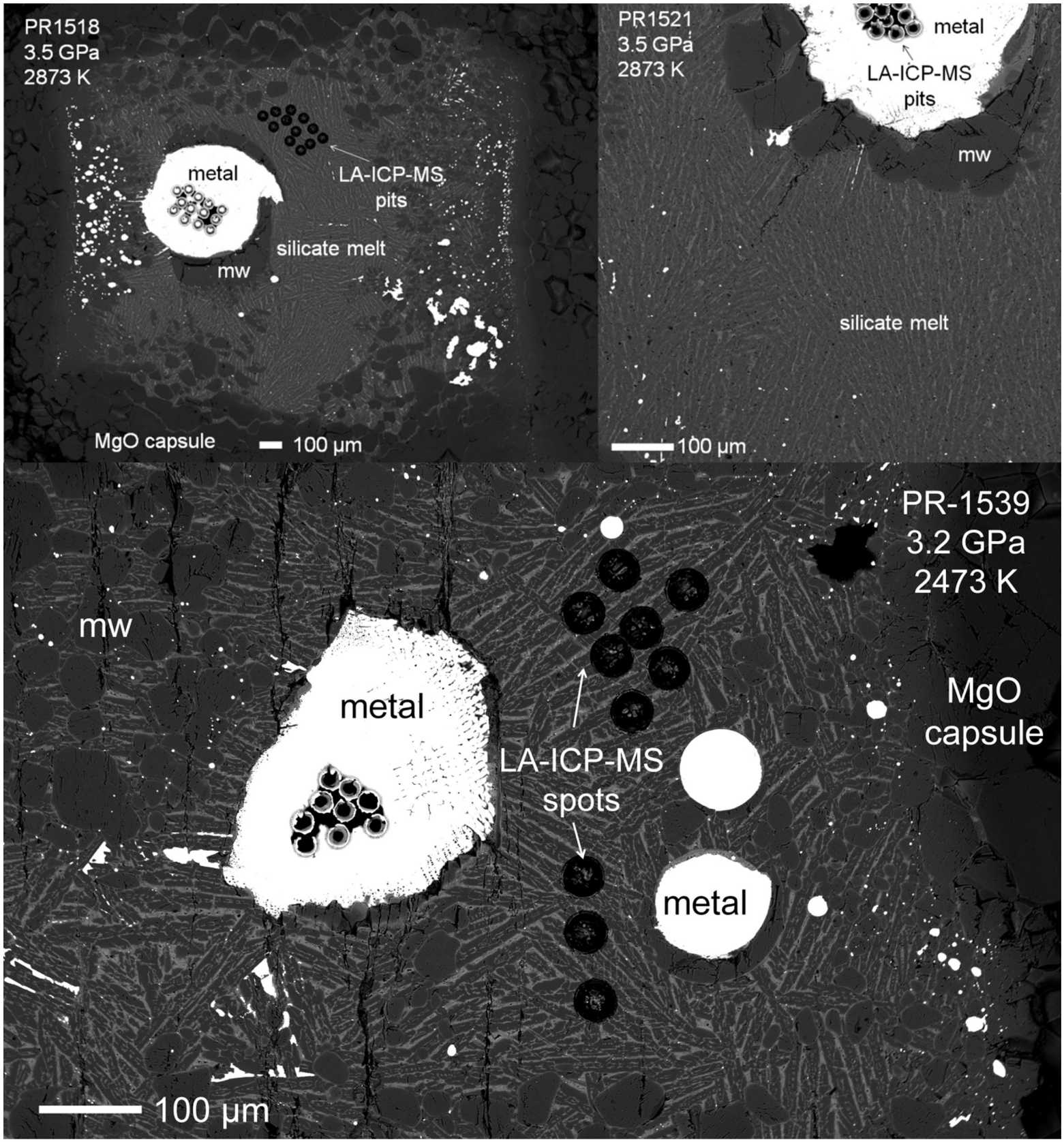
PR1518
3.5 GPa
2873 K
metal
LA-ICP-MS
pits
silicate melt
mw
MgO capsule
100 µm
PR1521
3.5 GPa
2873 K
metal
LA-ICP-MS
pits
mw
silicate melt
100 µm
PR-1539
3.2 GPa
2473 K
mw
metal
LA-ICP-MS
spots
metal
MgO
capsule
100 µm

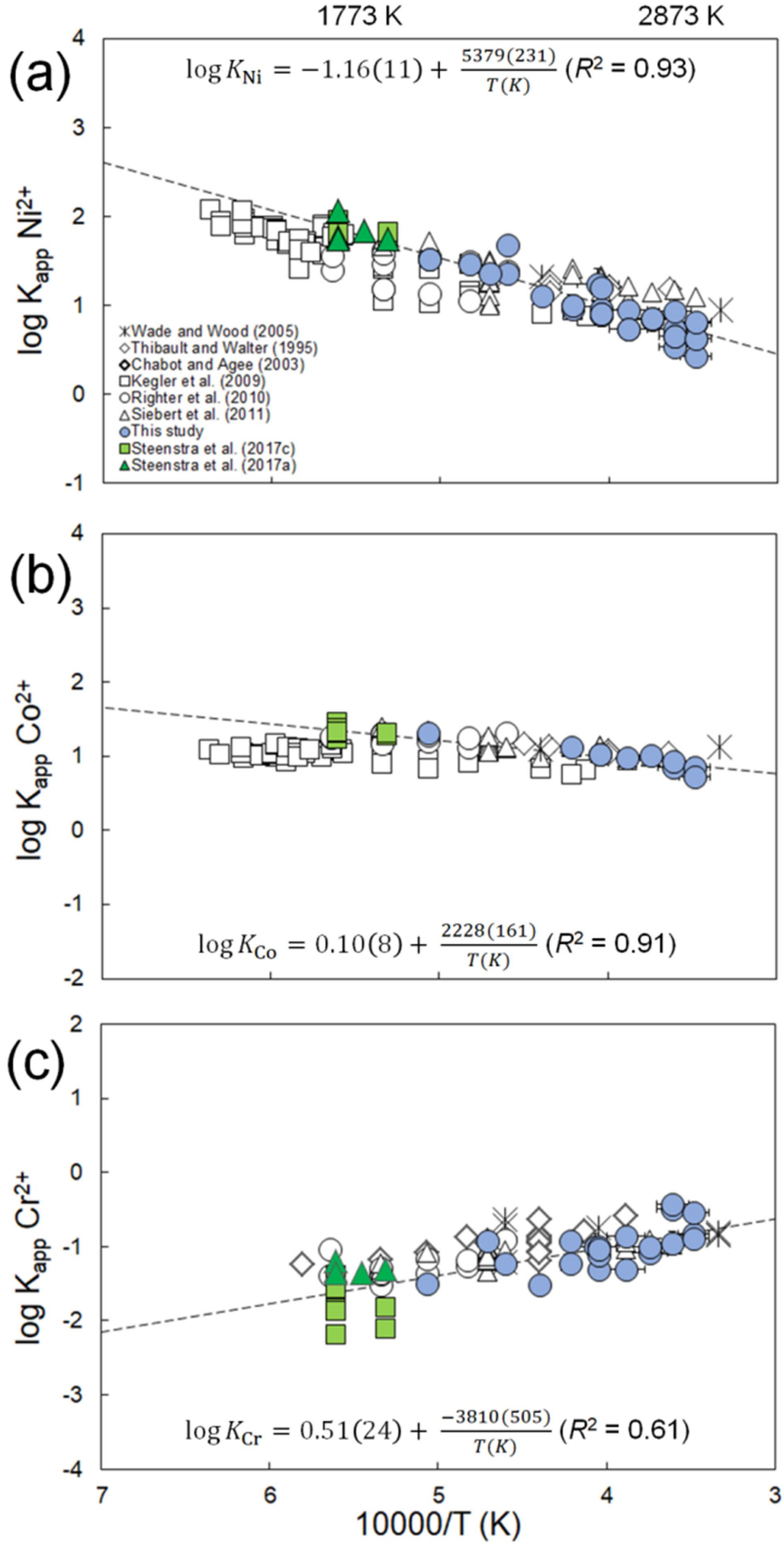
1773 K
2873 K
(a)
$\log K_{Ni} = -1.16(11) + \frac{5379(231)}{T(K)}$ (R^2 = 0.93)
log K_{app} Ni^{2+}
Wade and Wood (2005)
Thibault and Walter (1995)
Chabot and Agee (2003)
Kegler et al. (2009)
Righter et al. (2010)
Siebert et al. (2011)
This study
Steenstra et al. (2017c)
Steenstra et al. (2017a)
(b)
log K_{app} Co^{2+}
$\log K_{Co} = 0.10(8) + \frac{2228(161)}{T(K)}$ (R^2 = 0.91)
(c)
log K_{app} Cr^{2+}
$\log K_{Cr} = 0.51(24) + \frac{-3810(505)}{T(K)}$ (R^2 = 0.61)
10000/T (K)

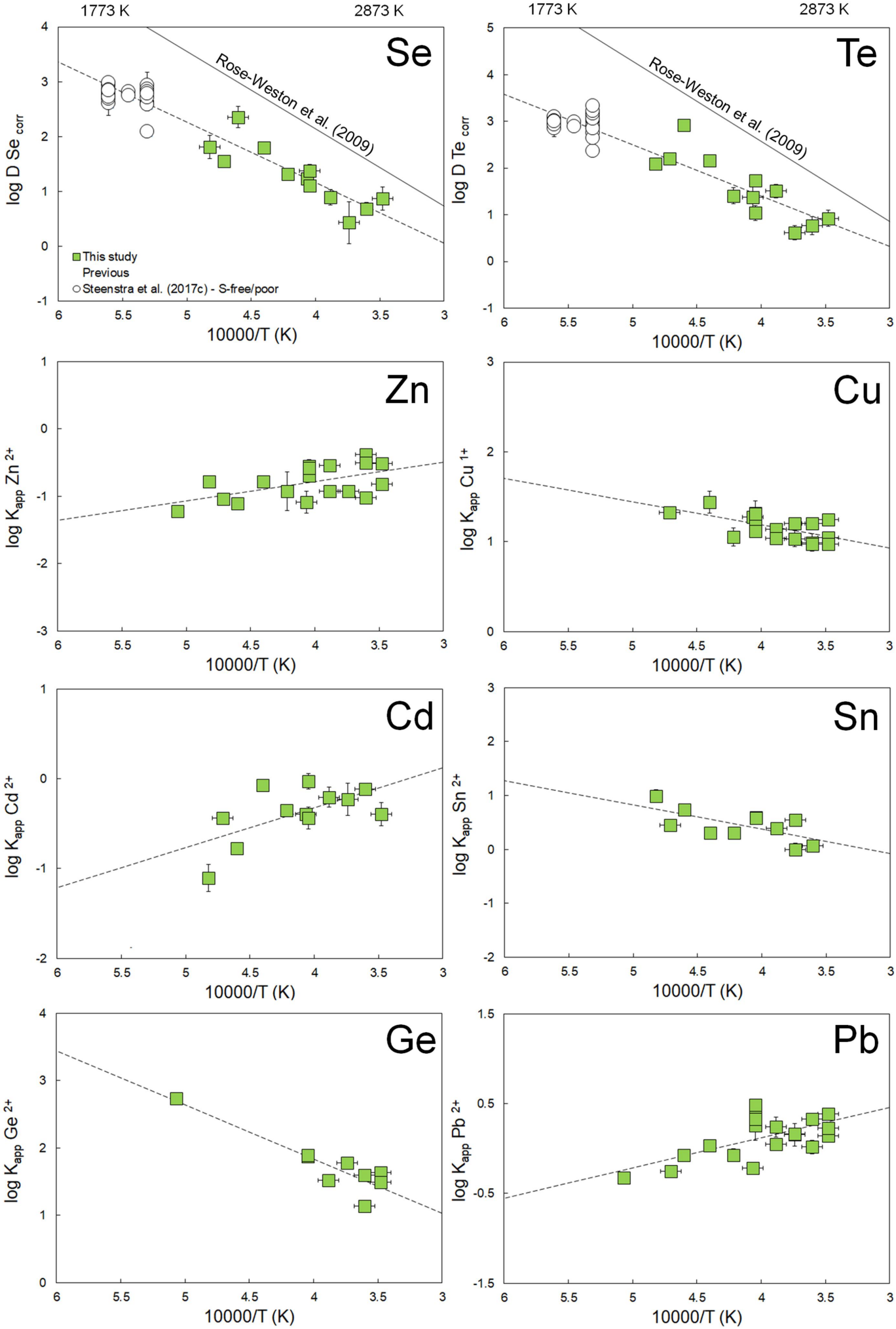
1773 K
2873 K
Se
Rose-Weston et al. (2009)
log D Se corr
This study
Previous
Steenstra et al. (2017c) - S-free/poor
10000/T (K)
Te
log D Te corr
Zn
log K app Zn 2+
Cu
log K app Cu 1+
Cd
log K app Cd 2+
Sn
log K app Sn 2+
Ge
log K app Ge 2+
Pb
log K app Pb 2+

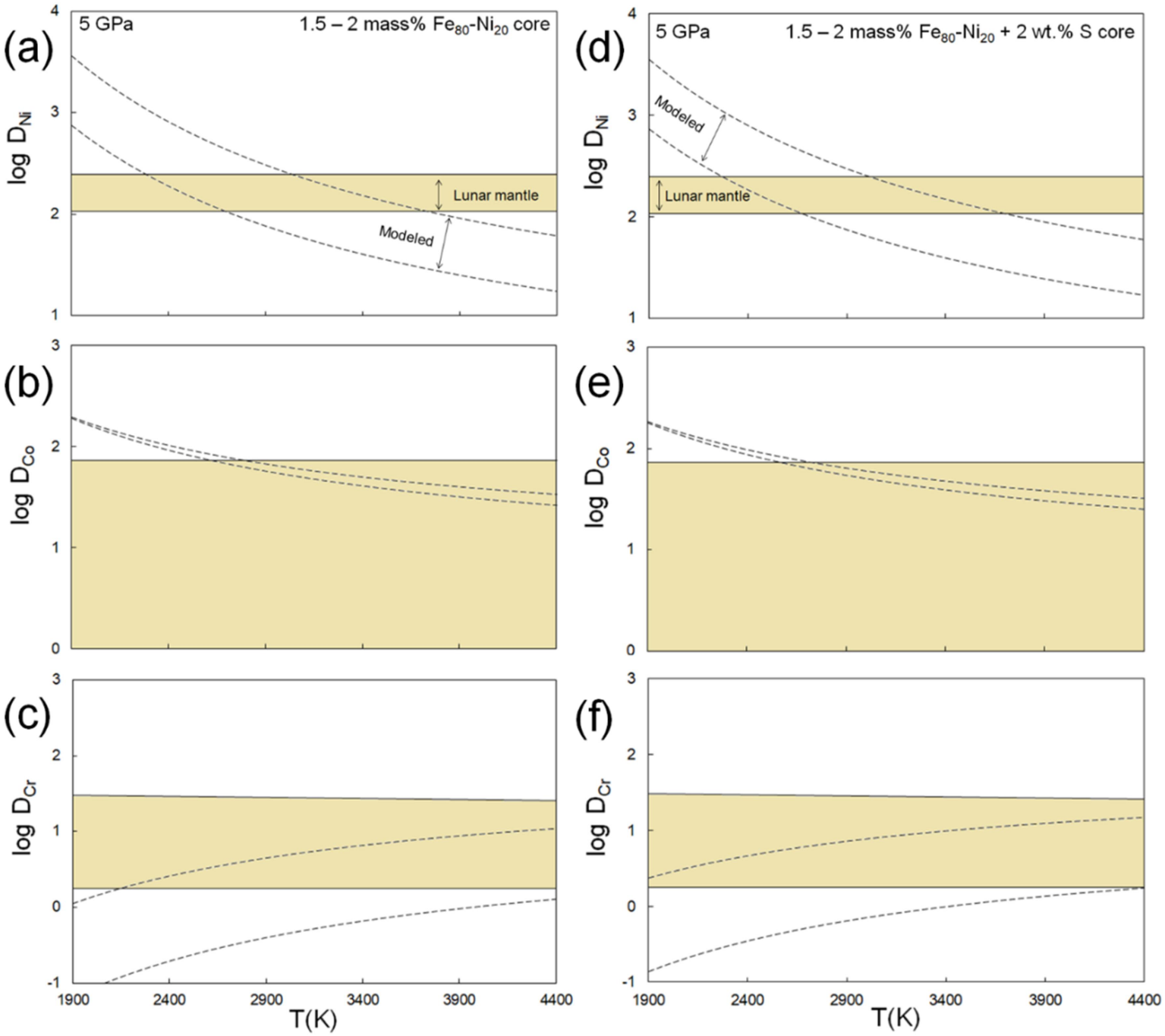
(a)
5 GPa
1.5 – 2 mass% Fe80-Ni20 core
log DNi
Lunar mantle
Modeled
(b)
log DCo
(c)
log DCr
T(K)
(d)
5 GPa
1.5 – 2 mass% Fe80-Ni20 + 2 wt.% S core
log DNi
Modeled
Lunar mantle
(e)
log DCo
(f)
log DCr
T(K)

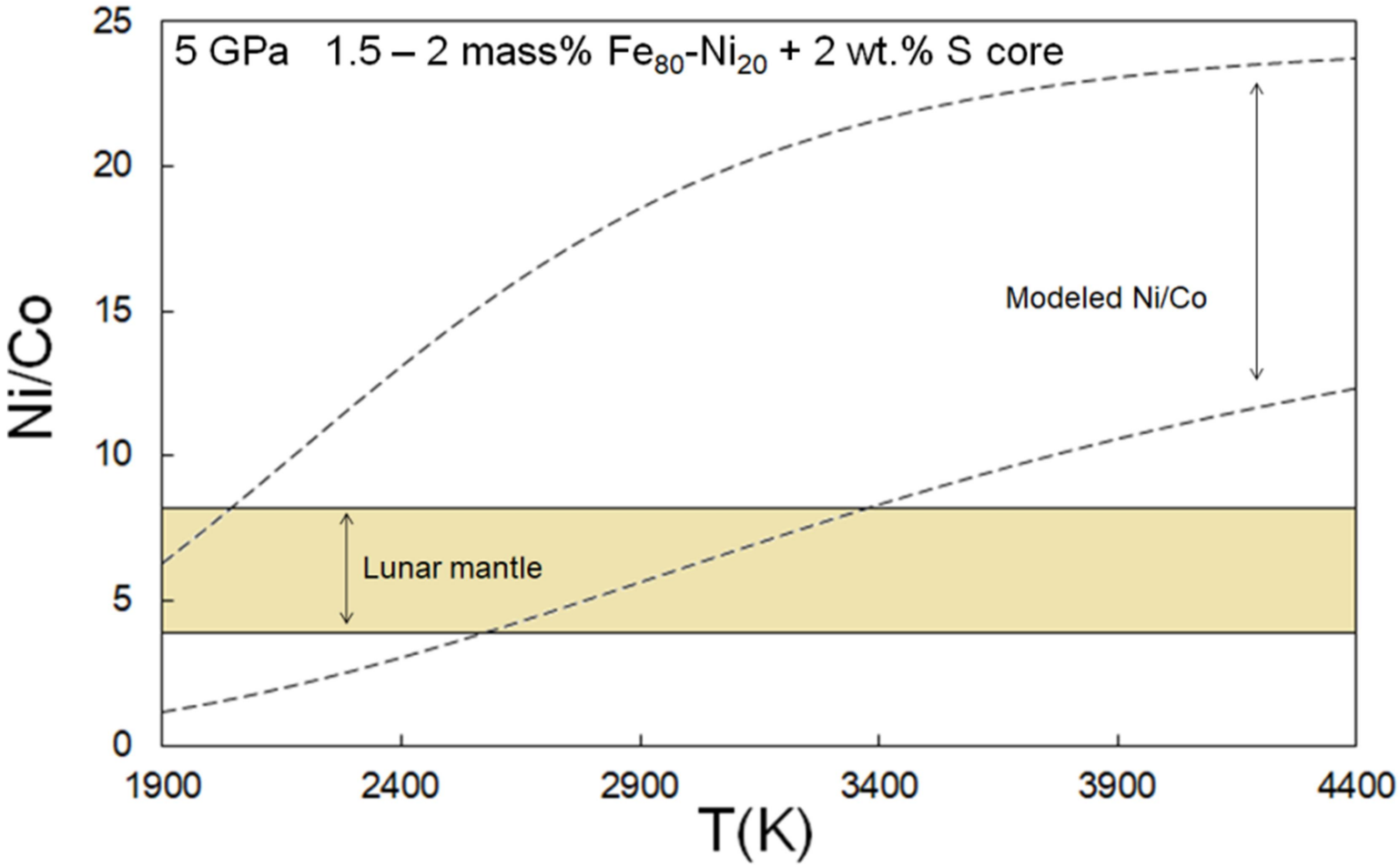
5 GPa 1.5 – 2 mass% Fe80-Ni20 + 2 wt.% S core
Modeled Ni/Co
Lunar mantle
Ni/Co
T(K)
0
5
10
15
20
25
1900
2400
2900
3400
3900
4400

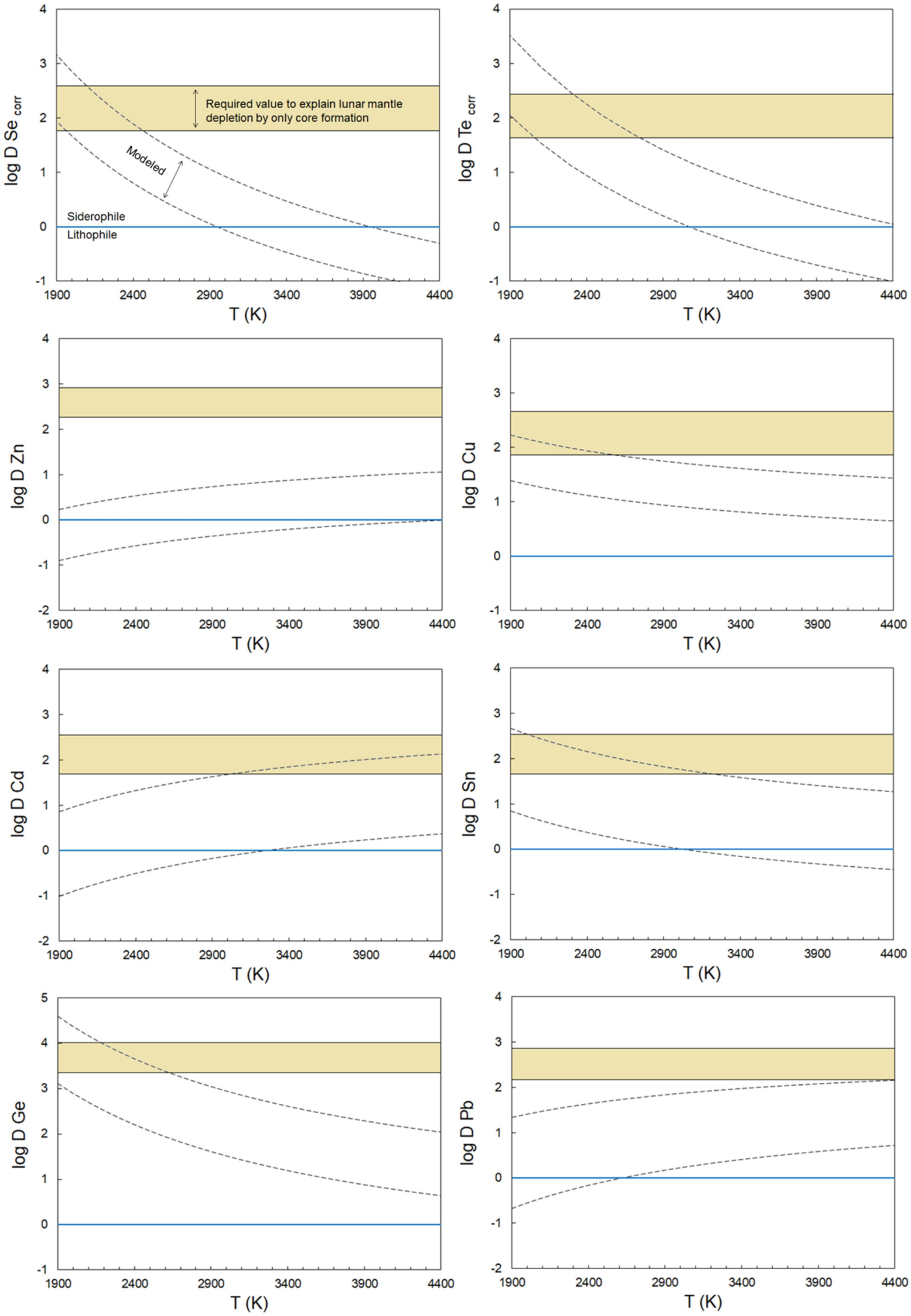
log D Se corr
Required value to explain lunar mantle depletion by only core formation
Modeled
Siderophile
Lithophile
T (K)
log D Te corr
T (K)
log D Zn
T (K)
log D Cu
T (K)
log D Cd
T (K)
log D Sn
T (K)
log D Ge
T (K)
log D Pb
T (K)

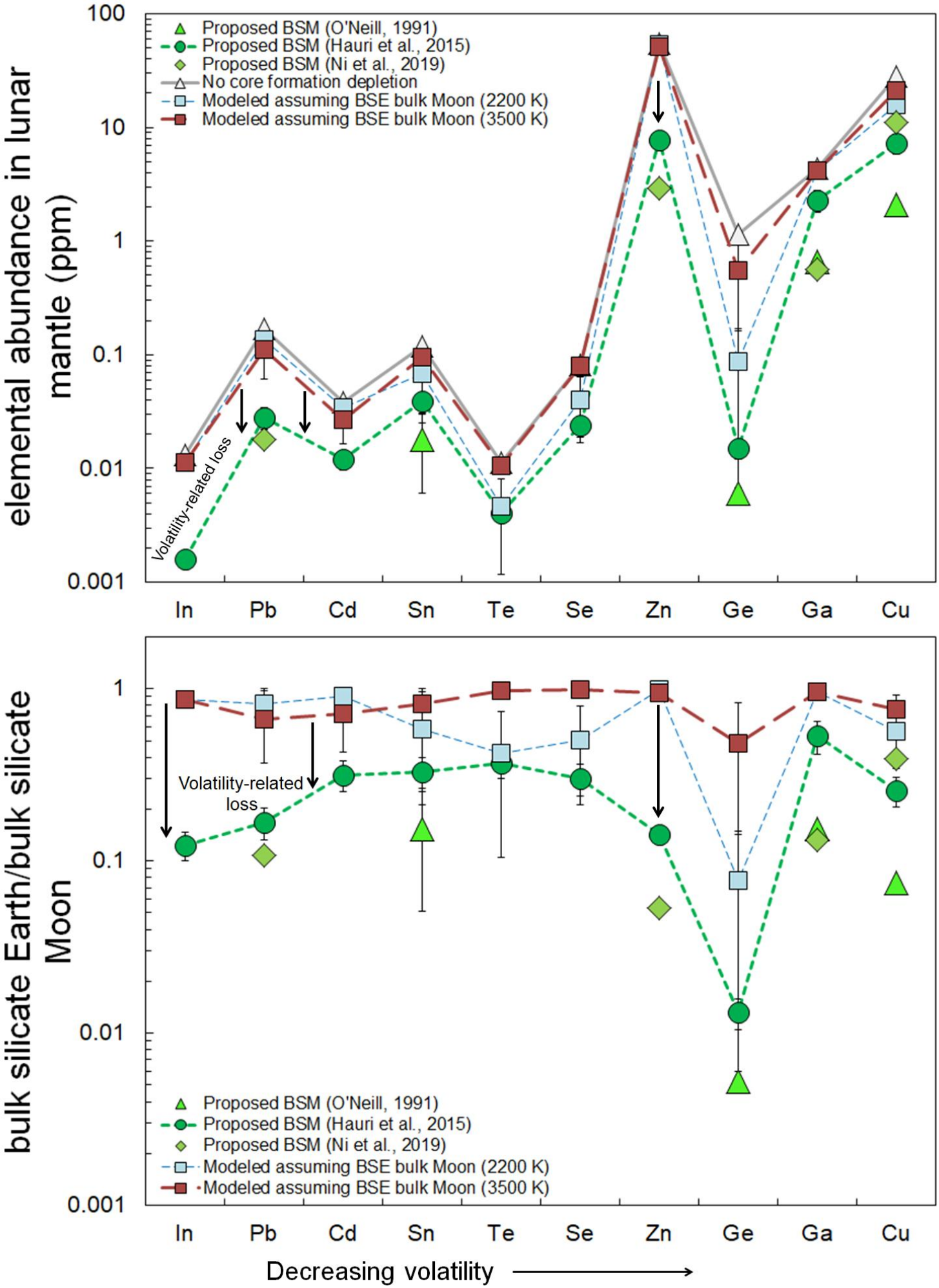
elemental abundance in lunar mantle (ppm)
100
10
1
0.1
0.01
0.001
Proposed BSM (O'Neill, 1991)
Proposed BSM (Hauri et al., 2015)
Proposed BSM (Ni et al., 2019)
No core formation depletion
Modeled assuming BSE bulk Moon (2200 K)
Modeled assuming BSE bulk Moon (3500 K)
Volatility-related loss
In
Pb
Cd
Sn
Te
Se
Zn
Ge
Ga
Cu
bulk silicate Earth/bulk silicate Moon
1
0.1
0.01
0.001
Volatility-related loss
Proposed BSM (O'Neill, 1991)
Proposed BSM (Hauri et al., 2015)
Proposed BSM (Ni et al., 2019)
Modeled assuming BSE bulk Moon (2200 K)
Modeled assuming BSE bulk Moon (3500 K)
In
Pb
Cd
Sn
Te
Se
Zn
Ge
Ga
Cu
Decreasing volatility

Supplementary information file for ''A possible high-temperature origin of the Moon and its geochemical consequences'' by E.S. Steenstra, J. Berndt, S. Klemme, Y. Fei and W. van Westrenen.

A.1 Quantification of run temperatures using power-*T* curves

At the pressures relevant for lunar core formation tungsten-rhenium thermocouples melt at ~2500 K. We therefore constrained the experimental run temperatures at temperatures that exceed the melting point of the thermocouple using well-defined power-temperature relationships, obtained at temperatures below the thermocouple melting point. For Cr-doped MgO octahedra at a hydraulic pressure of 109 bar (equivalent to a sample pressure of 3.8 GPa), experimental temperatures are calculated as a function of power (in Watts) using the following relationship (based on three experiments):

$$T(°C) = 1.94 * \text{power (W)} - 109 \qquad (R^2 = 0.99) \qquad (A.1)$$

For runs for which ZrO_2 octahedra were used, power-*T* curves yield (based on 16 experiments):

$$T(°C) = 2.41 * \text{power (W)} - 93 \qquad (R^2 = 0.98) \qquad (A.2)$$

Based on the variability in power-temperature relationships illustrated in Fig. S.1 we calculate an estimated uncertainty of ~50 K on calculated run temperatures for experiments performed in ZrO_2 octahedra and ~100 K for experiments performed in Cr-doped MgO octahedra (see main-text Table 1).

A.2 Details of EPMA analyses of experimental run products

Major and trace element concentrations in the run products were obtained using electron microprobes at the Institute of Mineralogy at the University of Munster and at the Dutch National Geological Facility at Utrecht University. Both institutes are equipped with a JEOL JXA 8530F field emission electron microprobe. Measurement points were set in lines and/or raster grids, depending of the available surface area of the analysed phases. The electron beam size was approximately equivalent to the step size (5–15 um), while using a beam current of 15 nA and an accelerating voltage of 15 kV. Dwell times of 20–30 s on peak and 10–15 s on each background were used. At least 20 repeat analyses were performed if sufficient sample surface area was available, and usually more (N > 30). Care was taken to avoid analyses of areas close to the edge of phases and/or surrounding capsule materials. Standards used for metal analyses were KTiPO5 or apatite for P, fayalite or pure Fe metal for Fe, TiO_2 or rutile for Ti, tephroite or rhodonite for Mn, pure metal or willemite for Zn, galena or Pb-Zn glass for Pb, pure

metal or InAs for In, GaAs or InAs for As, pure metal or CdS for Cd, hypersthene or diopside for Si, chalcopyrite or pyrite for S, pure metal or Cr_2O_3 for Cr, pure metal or NiO for Ni, and pure metal standards for V, Co, Cu, Ge, Se, Sn, Sb, Te, Mo and W. Elements Na, Si, Al, Se, Mg, As and Ge were measured on the TAP crystal; Ca, P, S, Mo, Sb, Cd, K, Sn, Ti on the PETJ crystal; V, Cr, Mn, Fe, Co, Ni, Cu, W, Zn on the LIFL crystal and Pb, Bi, In, Te on the PETH crystal.

Silicate melt reference materials for major and minor elements were diopside for Si, diopside for Ca, forsterite for Mg, corundum for Al, hematite for Fe, tephroite or MnO_2 for Mn, $KTiPO_5$ or orthoclase for K, GaP or $KTiPO_5$ for P, TiO_2 for Ti, jadeite for Na, galena for Pb, CdTe for Cd and Te, InAs for In, chalcopyrite or pyrite for S, and pure metal reference materials for Cr, Ni, Se, Cu, Zn and Sn. Calibrations were considered successful when the primary standard compositions were reproduced within 1% relative deviation. In Steenstra et al. (2019) we present a full analysis of the accuracy of our analytical strategy, using analyses of the NIST 610 reference glass with the EPMA standardization that was implemented in the previous studies that are used in this work. We observed that there is generally good agreement (i.e. within 10% relative deviation) between reference and measured values, despite the low ,concentrations of nominally 500 ppm and the use of a moderate beam current of 15 nA due to the beam sensitive nature of silicate glasses (Fig. S.3). Several analyses of the NIST 616 glass, that contains approximately 0.5 ppm of each trace element, were also performed to assess true zero counts for the elements of interest and confirmed the accuracy and precision of our analytical approach.

A.3 Corrections for matrix effects for LA-ICP-MS analyses of Fe-rich alloys

We have recently shown that the use of non-matrix matched silicate reference materials for analyses of volatile or highly refractory trace elements in Fe-rich metals may result in erroneous results (Steenstra et al., 2019). Although this issue does not affect the results discussed in this study due to the fact that the elements considered here are non-volatile it does affect the concentrations determined for other volatile and highly refractory trace elements in the metal alloys. To address this issue, we derived empirical correction terms by comparison of trace element measurements obtained by EPMA and LA-ICP-MS (Steenstra et al., 2019). We use the correction terms from the latter study to correct for the matrix effects.

A.4 Compositional effects on metal-silicate partitioning behavior of Mo and W

The metal-silicate partitioning behavior of Mo and W, like P, is strongly affected by variabilities in silicate melt composition (e.g. O'Neill and Eggins, 2002; Righter et al., 2010; Siebert et al., 2011; Steenstra et al., 2017). Given the strong correlation between increasing temperatures and increasing interaction of the silicate melt with the MgO capsule (Fig. S.4), observed temperature trends for Mo and W could be partly and/or fully the result of variations in silicate melt composition. Unfortunately, the exact effects

of each of the major element oxide on activities of Mo and W in the silicate melt are not well constrained and *cannot* be described using a single silicate compositional parameter such as nbo/t (O'Neill and Eggins, 2002) prohibiting a quantitative analysis of the effects of *T* on Mo and W metal-silicate partitioning. However, the individually determined $\mathrm{D}_{\mathrm{W}}^{\mathrm{met\ liq-sil\ melt}}$ values should be representative of that of lunar metal-silicate equilibrium. This is justified by the similar CaO contents of the bulk silicate Moon and those of the experimental silicate melts produced in the highest-*T* experiments, as it has been shown that $\mathrm{D}_{\mathrm{W}}^{\mathrm{met\ liq-sil\ melt}}$ most strongly varies as a function of CaO (O'Neill and Eggins, 2002; Steenstra et al., 2017).

A.5 Metal-silicate partitioning of W during high-*T* lunar differentiation

Thiemens et al. (2019) recently studied the Hf/W ratio of the Moon and suggested that a $\mathrm{D}_{\mathrm{W}}^{\mathrm{met\ liq-sil\ melt}}$ value of 60 would be required to explain the present-day Hf/W ratio of the lunar mantle. A temperature effect on $\mathrm{D}_{\mathrm{W}}^{\mathrm{met\ liq-sil\ melt}}$ could unfortunately not be derived in this study for lunar compositions due to strong correlations of silicate melt composition and temperature (Fig. S.4). The lack of a temperature effect on $\log K_{\mathrm{W}}$ for lunar melt compositions observed in this study could suggest that the temperature dependence of $\log \mathrm{D}_{\mathrm{w}}$ is indistinguishable from that of log D_{Fe}. In any case, the $\log \mathrm{D}_{\mathrm{w}}$ values measured for the highest temperature experiments (possessing similar silicate melt compositions and obtain within the range of proposed core formation temperatures) are consistent with the proposed Hf/W ratio of the silicate Moon for a 1.5% lunar core mass, showing that high-temperature core formation (as inferred from Ni and Co systematics) would reproduce the Hf/W of the lunar mantle (Fig. S.5; Thiemens et al., 2019).

A.6 Potential effects of late veneer on volatile siderophile/chalcophile element abundances in the lunar mantle

To illustrate the potential effects of a lunar late veneer on volatile siderophile and chalcophile element abundances, we assumed a 0.02 to 0.05 mass% (Kruijer et al., 2015) contribution of CI chondrites (the most volatile siderophile- and chalcophile element meteorite suite) or H chondrites to the lunar mantle, while using the bulk compositional estimates of Alexander (2019) and Newsom (1995) and references therein. The results suggests that the majority of the lunar mantle abundances (except of Ge and to a lesser extent Se and Te) would remain unaffected by a late veneer, especially given the likely degassing of such elements following impact.

Supplementary references

Alexander C.M.O.D. (2019) Quantitative models for the elemental and isotopic fractionations in chondrites: The carbonaceous chondrites. *Geochim. Cosmochim. Acta* **254,** 277–309.

Alexander C.M.O.D. (2019) Quantitative models for the elemental and isotopic fractionations in chondrites: The non-carbonaceous chondrites. *Geochim. Cosmochim. Acta* **254,** 246–276.

Newsom HE (1995) Composition of the Solar System, Planets, Meteorites, and Major Terrestrial Reservoirs. In Global Earth Physics: A Handbook of Physical Constants, AGU Reference Shelf volume 1 (ed. T. J. Ahrens), pp. 159–189. American Geophysical Union, Washington, D.C.

O'Neill H.S.C., Eggins S.M. (2002) The effect of melt composition on trace element partitioning: an experimental investigation of the activity coefficients of FeO, NiO, CoO, MoO2 and MoO3 in silicate melts. *Chem. Geol.* **186**, 151–181.

Righter K, Pando K. M., Danielson L., Lee C. T. (2010) Partitioning of Mo, P and other siderophile elements (Cu, Ga, Sn, Ni, Co, Cr, Mn, V, and W) between metal and silicate melt as a function of temperature and silicate melt composition. *Earth Planet. Sci. Lett.* **291**, 1–9.

Siebert J., Corgne A., Ryerson F.J. (2011) Systematics of metal-silicate partitioning for many siderophile elements applied to Earth's core formation. *Geochim. Cosmochim. Acta*. **75**, 1451–1489.

Steenstra E.S., Sitabi A.B., Lin Y.H., Rai N., Knibbe J.S., Berndt J., Matveev S., van Westrenen, W. (2017) The effect of melt composition on metal-silicate partitioning of siderophile elements and constraints on core formation in the angrite parent body. *Geochim. Cosmochim. Acta*. **212,** 62–83.

Steenstra E.S., Berndt J., Klemme S., van Westrenen W. (2019) LA-ICP-MS analyses of Fe-rich alloys: quantification of matrix effects for 193 nm excimer laser systems. *J. Analytical Atom. Spectrometr.* **34**, 222–231.

Thiemens M.W., Sprung P., Fonseca R.O.C., Leitzke F.P., Munker C. (2019) Early Moon formation inferred from hafnium-tungsten systematics. Nat. Geosci., doi:10.1038/s41561-019-0398-3.

Fig. S.1 Power temperature relationships derived from experiments performed using thermocouples for experiments conducted using Cr-doped MgO octahedra (left) and ZrO_2 octahedra (right).

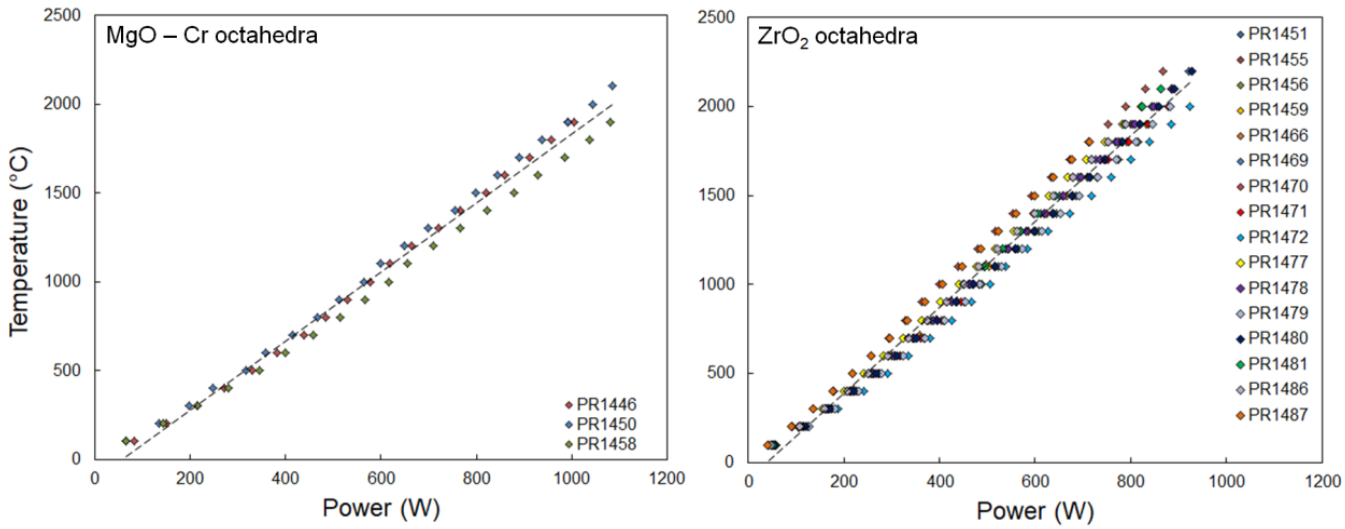

Fig. S.2 Comparison between measured and reported trace elements (GeoRem database, Application Version 19 and references therein) determined for NIST-610 and GSD-1G using different beam sizes (from Steenstra et al. 2019, but measured in between sessions in which samples from this study were analysed).

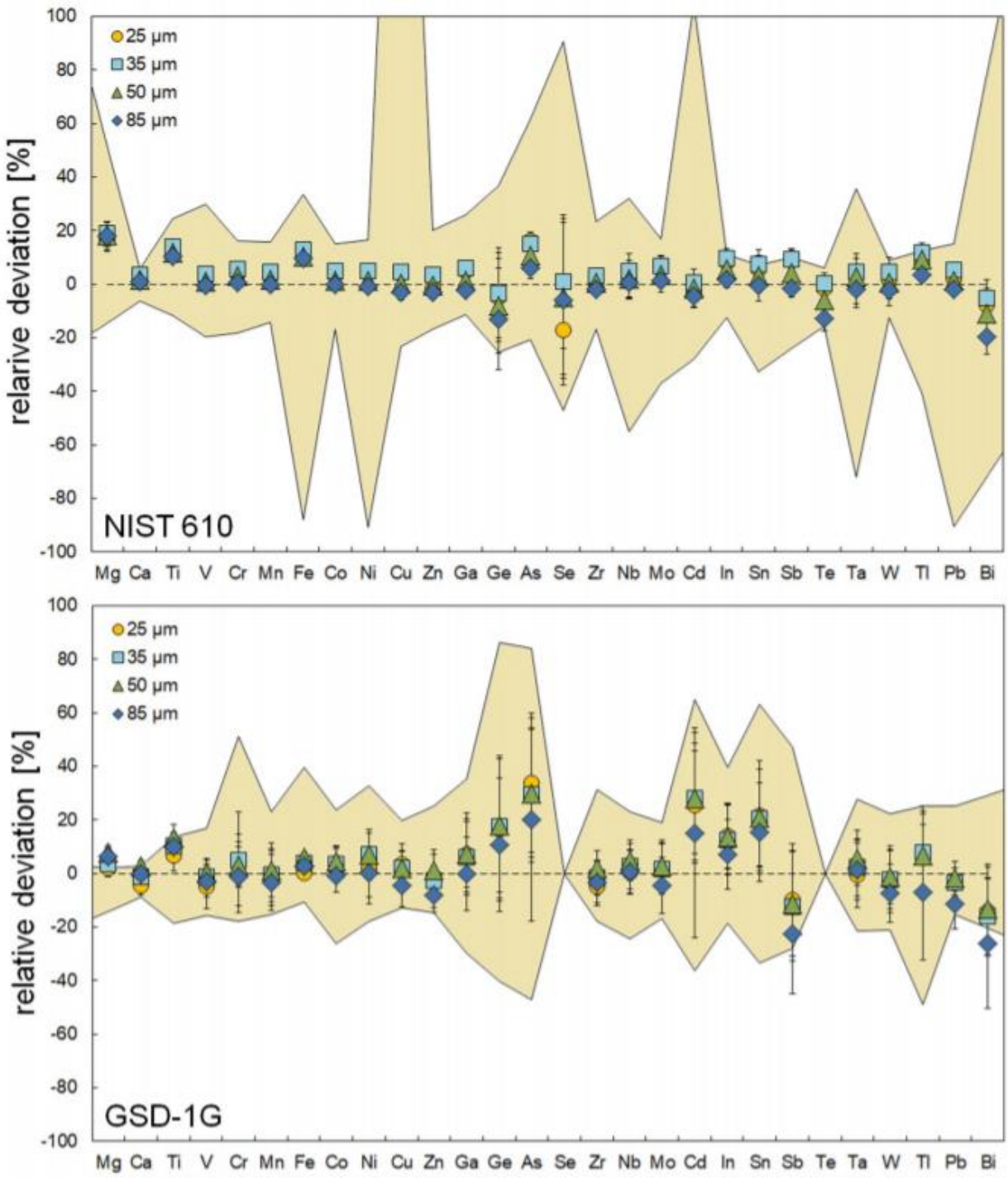

Fig. S.3 Relative deviations between reference concentrations of silicate reference material NIST 610 (taken from the GeoRem database website) and those measured by electron microprobe in this study. Shaded area represents the range of published data, dotted lines define 10% relative deviation. All uncertainties are 1 standard deviation (figure from Steenstra et al. 2019, but measured in between sessions in which samples from this study were analysed).

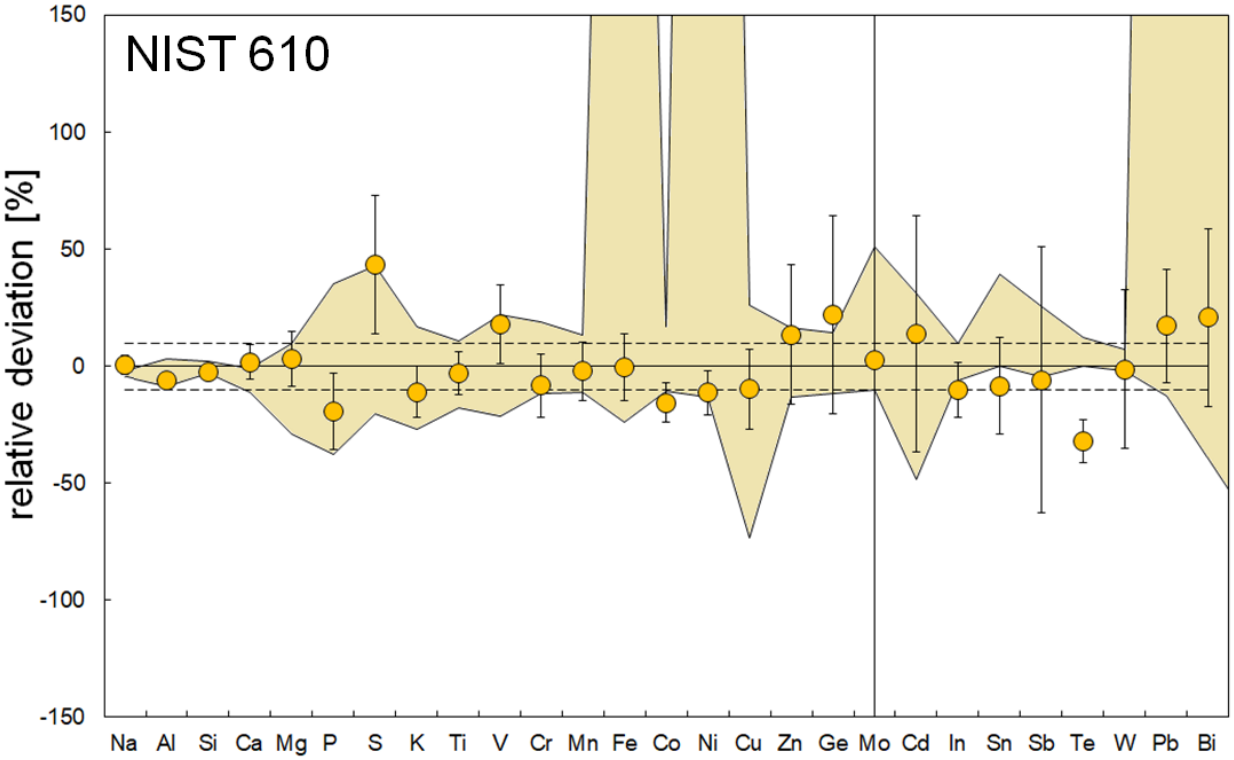

Fig. S.4 Correlation between experimental peak temperature and abundance of major element oxides in the silicate melt. Crosses indicate initial major oxide concentrations prior to experiment.

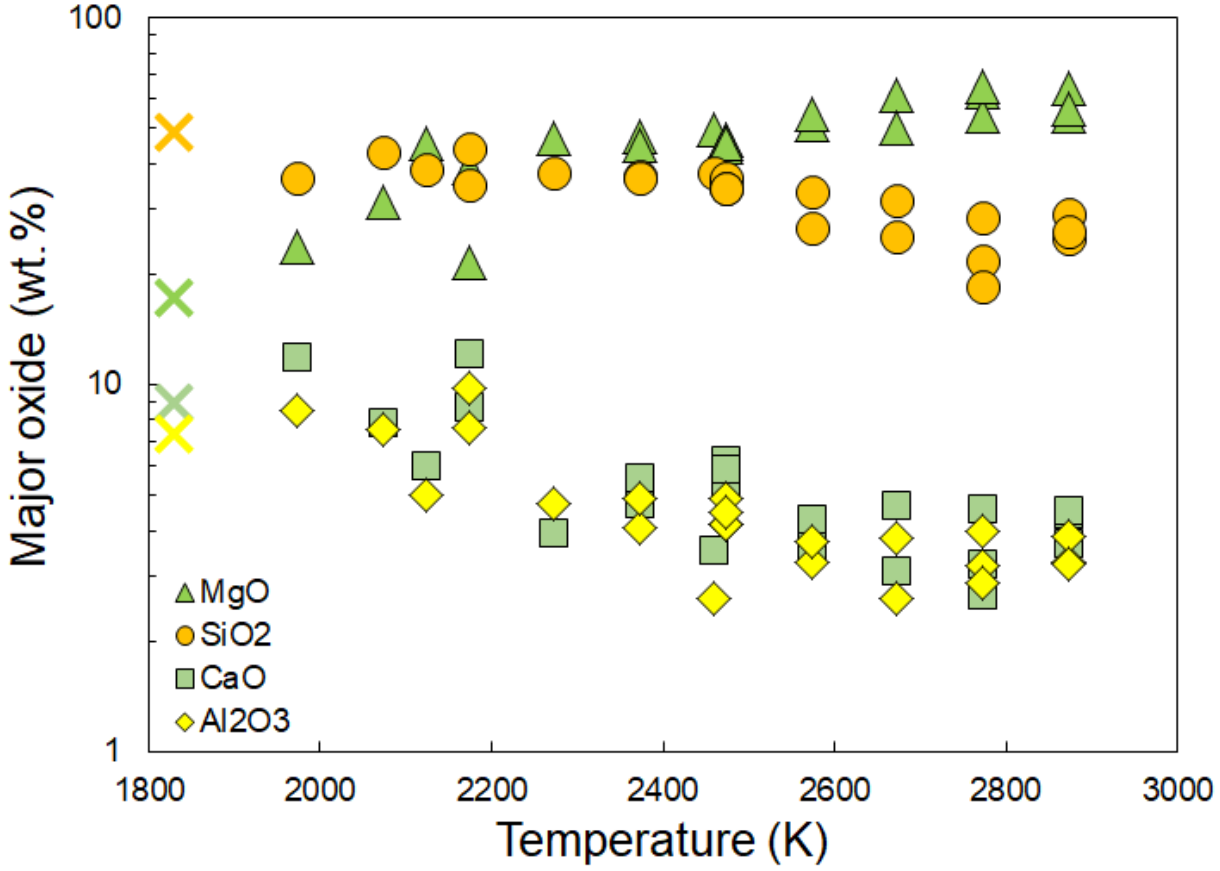

Figure S.5 Log $D_W^{\text{met liq-sil melt}}$ values from this study as a function of temperature. Values were normalized to a lunar fO_2 of 2 units below the iron-wüstite buffer (Steenstra et al., 2016) assuming a valence state of 6+ for W (Siebert et al., 2011). Horizontal line indicates the minimum estimate of log $D_W^{\text{met liq-sil melt}}$ during lunar core formation required for explaining the Hf/W ratio of the silicate Moon (Thiemens et al., 2019).

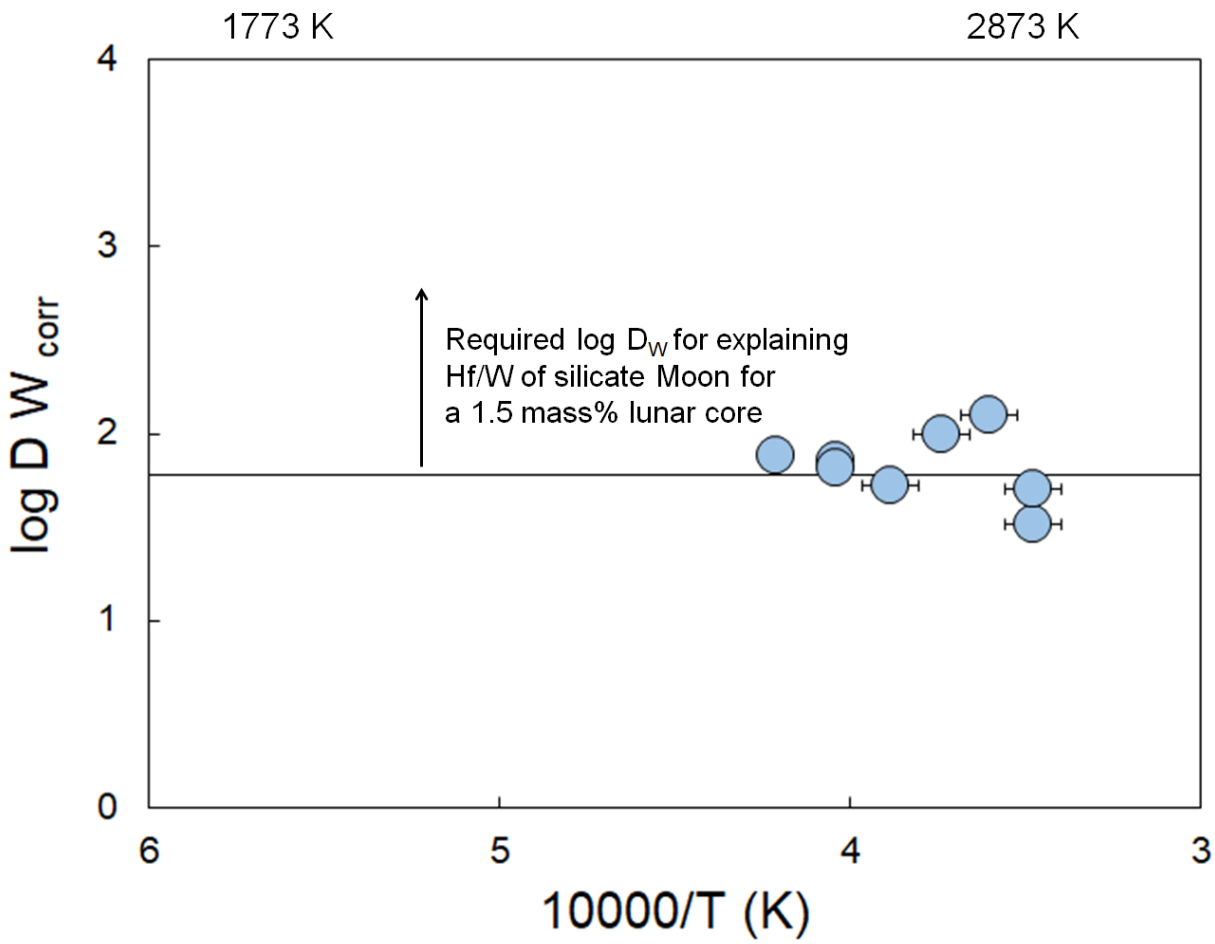

Table S.1 Silicate compositions of experimental charges determined by EPMA and LA-ICP-MS.

Run #	PR1446	PR1449	PR1450	PR1465	PR1468	PR1470	PR1477	PR1480	PR1481	PR1489	PR1491	PR1505	PR1506	PR1508
EPMA (wt.%)	*N = 35* [a]	*N = 29*	*N = 32*	*N = 29*	*N = 38*	*N = 65*	*N = 28*	*N = 19*	*N = 30*	*N = 30*	*N = 61*	*N = 15*	*N = 24*	*N = 16*
MgO	39.08(271)[b]	45.25(264)	47.42(110)	49.75(197)	32.23(150)	44.23(200)	46.66(192)	46.21(195)	45.02(122)	51.04(359)	61.79(187)	50.00(174)	54.40(213)	63.97(139)
SiO_2	35.00(90)	38.76(75)	37.00(107)	37.95(161)	43.02(29)	34.12(156)	37.81(100)	35.67(166)	36.65(62)	33.59(266)	25.41(194)	31.80(243)	26.65(187)	24.97(142)
Al_2O_3	7.58(119)	4.99(111)	4.05(76)	2.60(142)	7.31(54)	4.14(102)	4.75(145)	4.15(95)	4.90(70)	3.28(136)	2.60(36)	3.79(80)	3.72(52)	3.26(24)
CaO	8.65(154)	6.02(167)	4.76(73)	3.54(130)	7.46(67)	5.43(133)	3.93(87)	5.39(112)	5.56(68)	4.27(221)	3.10(47)	4.70(104)	3.61(49)	3.68(32)
FeO	7.80(68)	4.30(49)	4.55(41)	4.56(62)	8.78(14)	7.37(87)	6.05(67)	6.19(89)	5.89(34)	4.83(81)	4.56(41)	7.19(87)	7.28(57)	4.97(28)
K_2O	0.014(5)	0.01(1)	0.03(1)	0.006(3)	0.023(3)	0.01(1)	0.009(3)	0.02(1)	0.010(3)	0.02(1)	0.010(2)	0.006(3)	0.03(1)	n.d.
Na_2O	0.03(1)	0.03(1)	0.61(13)	0.31(13)	0.08(1)	0.05(1)	0.016(5)	0.65(12)	0.15(7)	0.08(1)	0.61(11)	0.29(7)	1.51(29)	n.d.
MnO	0.18(2)	0.14(1)	0.10(1)	0.06(1)	0.19(1)	0.74(7)	0.12(1)	0.10(1)	1.00(6)	0.09(1)	0.049(4)	0.85(6)	0.66(2)	0.07(3)
Cr_2O_3	0.24(2)	0.16(2)	0.10(2)	0.05(3)	0.30(1)	0.65(13)	0.21(4)	0.12(3)	0.83(10)	0.09(3)	0.07(1)	0.73(15)	0.71(8)	0.13(3)
V_2O_3	–	–	–	–	–	0.68(13)	–	–	0.92(10)	–	–	1.28(25)	0.75(7)	–
TiO_2	0.24(4)	0.16(4)	0.13(2)	0.07(3)	0.21(1)	0.15(4)	0.13(3)	0.14(3)	0.14(2)	0.11(4)	0.06(1)	0.11(2)	0.10(2)	0.09(1)
NiO	0.01(1)	0.008(4)	0.02(1	0.007(3)	0.009(4)	0.011(3)	0.01(1)	0.01(1)	0.011(5)	0.02(1)	0.010(3)	0.007(4)	0.01(1)	0.01(1)
CoO	–	–	–	–	–	0.02(1)	–	–	0.012(4)	–	–	0.02(1)	0.03(1)	–
P_2O_5	–	–	–	–	–	0.06(2)	–	–	0.03(1)	–	–	0.06(2)	0.06(2)	–
In_2O_3	0.11(2)	0.11(2)	0.10(2)	0.06(2)	0.11(1)	–	0.08(1)	0.06(2)	–	n.d. [d]	0.09(1)	–	–	0.10(1)
CdO	0.24(5)	0.08(2)	0.11(4)	0.03(1)	0.30(3)	–	0.06(2)	0.06(5)	–	0.09(9)	0.07(2)	–	–	n.d.
SeO2	0.07(3)	0.01(1)	0.06(3)	0.03(2)	0.004(3)	–	b.d.l.[c]	0.26(8)	–	0.19(18)	0.75(12)	–	–	0.37(7)
TeO2	0.002(2)	b.d.l.	0.02(1)	0.006(4)	0.002(2)	–	b.d.l.	0.24(5)	–	n.d.	0.25(5)	–	–	0.01(2)
PbO	0.09(3)	0.03(1)	0.06(2)	0.02(2)	0.15(2)	–	0.03(2)	0.03(2)	–	0.04(3)	0.03(1)	–	–	0.02(1)
SO_3	0.01(1)	0.20(9)	0.13(6)	0.02(1)	0.20(7)	0.012(3)	0.009(3)	0.01(1)	0.01(1)	0.016(5)	0.10(5)	b.d.l.	0.01(1)	0.004(3)
ZrO_2	0.11(2)	0.008(4)	0.24(4)	0.20(6)	0.14(1)	0.02(1)	0.04(1)	0.01(1)	0.05(1)	b.d.l. [c]	0.03(1)	0.05(2)	0.02(1)	n.d.
Total	99.45(28)	100.06(29)	99.34(35)	99.28(42)	100.56(15)	97.75(28)	99.97(25)	99.34(50)	101.24(26)	97.78(53)	99.62(35)	100.96(42)	99.61(53)	101.64(22)
LA–ICP–MS	*N = 13*	*N = 9*	*N = 25*	*N = 5*	*N = 10*	*N = 13*	*N = 8*	*N = 8*	*N = 11*	*N = 13*	*N = 12*	*N = 10*	*N = 11*	*N = 11*
	–	–	–	–	–	*N (P) = 7*	–	–	*N (P) = 9*	–	–	*N (P) = 6*	*N (P) = 7*	–
CaO (wt.%)	7.62(63)	6.86(78)	5.42(24)	4.87(123)	8.69(14)	5.76(26)	6.31(104)	4.68(37)	6.19(29)	4.51(15)	3.24(29)	5.32(23)	3.56(11)	3.64(13)
Ti (ppm)	1378(86)	1190(124)	953(40)	704(207)	1467(20)	906(34)	1052(167)	751(51)	969(42)	706(33)	526(39)	832(33)	581(17)	613(21
P	–	–	–	–	–	117(7)	–	–	154(27)	–	–	197(11)	223(12)	–
V	–	–	–	–	–	5010(158)	–	–	6640(212)	–	–	9836(427)	5045(203)	–
Cr	1518(38)	1176(73)	651(35)	298(86)	2193(28)	4949(155)	1475(95)	916(136)	5718(195)	627(57)	737(93)	5335(235)	4585(216)	647(37)
Mn	1354(62)	1213(65)	838(25)	518(100)	1583(6)	6024(156)	1175(114)	809(48)	7977(246)	744(29)	518(39)	7061(211)	4870(102)	541(16)
Co	–	–	–	–	–	93(4)	–	–	41(4)	–	–	84(4)	113(4)	–
Ni	43(2)	22(1)	71(11)	38(12)	37(1)	32(2)	64(4)	78(17)	10(2)	76(11)	112(18)	33(2)	54(3)	126(21)
Cu	1.26(21)	1.6(2)	3.5(7)	2.0(2)	6.6(9)	2.7(2)	1.7(4)	2.3(6)	0.62(8)	2.7(4)	3.8(7)	1.34(17)	1.8(2)	2.5(7)
Zn	16(1)	13(1)	12(6)	13(4)	32(1)	20(1)	20(2)	14(1)	18(7)	6.9(5)	13(2)	16(1)	13(1)	8.6(5)
Ga	1.26(11)	1.45(12)	1.13(8)	1.8(7)	1.6(1)	1.11(6)	1.30(22)	0.73(6)	0.92(8)	0.60(4)	0.68(11)	1.17(10)	0.74(5)	0.56(5)
Ge	–	–	–	–	–	21(1)	–	–	5.9(23)	–	–	29(3)	45(4)	–
As	b.d.l.	2.0(8)	2.4(5)	9.7(43)	2.0(5)	–	2.9(2)	5.2(6)	–	1.83(19)	4.4(8)	–	–	10(4)
Se	673(44)	519(52)	925(44)	510(102)	321(7)	–	484(69)	965(123)	–	1761(151)	3813(904)	–	–	2638(193)
Zr	665(48)	56(6)	1846(115)	2883(1042)	979(25)	215(10)	337(57)	55(3)	357(21)	57(2)	155(11)	317(14)	61(12)	52(3)
Mo	–	–	–	–	–	13(2)	–	–	11(2)	–	–	28(2)	47(4)	–
Cd	2338(203)	1689(168)	1503(145)	665(132)	3467(65)	–	1607(207)	1013(200)	–	998(64)	1263(165)	–	–	1085(107)
In	948(71)	1506(145)	1004(125)	912(190)	966(12)	–	936(138)	732(130)	–	494(39)	1095(213)	–	–	768(127)
Sn	0.15(2)	0.30(4)	0.22(5)	b.d.l.	0.17(4)	0.15(3)	0.36(6)	<0.24	b.d.l.	<0.08(1)	0.31(7)	0.11(2)	0.14(3)	<0.09(1)
Sb	3.3(5)	3.3(7)	16(3)	4.3(36)	1.25(10)	–	24(4)	21(4)	–	6.0(15)	3.8(10)	–	–	26(8)
Te	206(15)	74(6)	427(51)	150(35)	63(2)	–	122(15)	1699(279)	–	524(57)	2197(510)	–	–	1168(212)
W	–	–	–	–	–	141(14)	–	–	81(8)	–	–	91(11)	163(26)	–
Pb	950(102)	829(90)	605(90)	261(37)	1556(19)	0.28(3)	689(84)	303(70)	0.30(5)	320(42)	344(44)	0.36(3)	0.18(2)	401(115)

Run #	PR1510	PR1517	PR1518	PR1521	PR1522	PR1524	PR1538	PR1539	PR1561
EPMA (wt.%)	*N = 26*	*N = 29*	*N = 29*	*N = 33*	*N = 30*	*N = 26*	*N = 30*	*N = 29*	*N = 25*

MgO	54.22(170)	65.10(209)	53.80(127)	56.95(209)	46.63(134)	62.70(240)	23.72(120)	45.17(143)	21.46(77)
SiO_2	28.48(185)	18.44(226)	29.19(156)	25.76(242)	36.38(96)	21.76(213)	36.47(61)	34.41(123)	44.19(51)
Al_2O_3	3.97(57)	2.87(31)	3.84(50)	3.23(41)	4.88(88)	3.20(48)	8.52(49)	4.48(90)	9.73(52)
CaO	4.61(70)	2.65(48)	4.42(59)	4.43(63)	6.20(89)	3.23(38)	11.82(76)	5.91(75)	12.19(39)
FeO	7.13(58)	9.13(58)	7.66(50)	7.40(59)	5.49(46)	7.58(37)	11.96(44)	7.56(64)	10.02(52)
K_2O	0.008(4)	0.003(2)	0.007(2)	0.004(2)	0.009(3)	0.002(1)	0.012(2)	0.004(2)	0.007(3)
Na_2O	0.15(3)	0.01(1)	0.03(1)	0.010(3)	0.02(1)	0.01(1)	0.030(5)	0.03(1)	0.017(4)
MnO	0.64(3)	0.54(1)	0.59(2)	0.64(2)	0.12(1)	0.06(1)	2.09(8)	1.14(6)	0.23(1)
Cr_2O_3	0.71(9)	0.64(5)	0.62(6)	0.61(7)	0.13(3)	0.11(1)	1.94(18)	0.87(16)	0.47(2)
V_2O_3	0.75(9)	0.73(4)	0.65(6)	0.71(7)	–	–	2.06(14)	1.01(18)	–
TiO_2	0.12(2)	0.08(1)	0.12(2)	0.10(1)	0.17(2)	0.08(1)	0.30(2)	0.15(3)	0.30(2)
NiO	0.02(1)	0.02(1)	0.013(5)	0.013(4)	0.02(1)	0.015(5)	0.008(4)	0.008(3)	0.01(1)
CoO	0.02(1)	0.05(1)	0.03(1)	0.03(1)	–	–	0.02(1)	0.02(1)	–
P_2O_5	0.02(1)	0.01(1)	0.02(1)	0.01(1)	–	–	0.06(1)	0.03(1)	–
In_2O_3	–	–	–	–	0.04(1)	0.05(1)	–	–	0.09(1)
CdO	–	–	–	–	0.08(3)	0.05(2)	–	–	0.48(3)
SeO2	–	–	–	–	0.15(5)	0.16(6)	–	–	0.005(4)
TeO2	–	–	–	–	0.01(1)	0.04(2)	–	–	b.d.l.
PbO	–	–	–	–	0.03(1)	0.02(1)	–	–	0.13(3)
SO_3	0.02(1)	0.01(1)	0.009(4)	0.01(1)	0.01(1)	0.013(5)	0.009(4)	0.01(1)	0.01(1)
ZrO_2	0.06(2)	0.03(1)	0.01(1)	0.02(1)	0.04(1)	0.02(1)	0.13(2)	0.05(2)	0.17(2)
Total	101.00(44)	100.39(32)	101.10(21)	100.00(22)	100.40(19)	99.11(41)	99.23(16)	100.93(26)	99.53(11)
LA–ICP–MS	*N = 15*	*N = 11*	*N = 12*	*N = 12*	*N = 10*	*N = 3*	*N = 10*	*N = 10*	*N = 14*
	N (P) = 10	*N (P) = 7*	*N (P) = 7*	*N (P) = 6*	–	–	*N (P) = 7*	*N (P) = 8*	–
CaO (wt.%)	4.74(11)	2.60(18)	4.91(15)	4.13(15)	4.99(22)	3.11(34)	12.88(59)	5.24(30)	11.95(18)
Ti (ppm)	818(20)	442(21)	823(27)	669(17)	825(28)	504(54)	2080(84)	864(36)	1959(50)
P	77(4)	60(5)	102(6)	85(11)	–	–	226(20)	126(6)	–
V	5372(218)	4660(644)	5243(225)	6333(535)	–	–	14875(652)	7126(321)	–
Cr	4782(209)	3875(668)	4712(219)	5212(490)	972(98)	690(18)	12230(570)	5853(259)	3339(63)
Mn	5013(128)	5259(971)	5011(108)	5664(365)	853(32)	506(46)	16696(549)	8594(222)	1858(31)
Co	98(4)	159(19)	150(6)	209(17)	–	–	71(3)	94(5)	–
Ni	45(2)	83(10)	71(4)	108(8)	46(5)	250(78)	12(1)	33(2)	28(1)
Cu	2.3(3)	1.27(17)	1.8(1)	1.9(1)	2.1(3)	6.1(12)	2.0(2)	0.80(12)	1.18(10)
Zn	14(1)	9.6(17)	17(1)	12(1)	11(1)	11(1)	37(2)	14.4(4)	33(1)
Ga	1.15(6)	0.44(4)	0.67(5)	0.65(4)	0.77(3)	0.77(11)	1.7(1)		1.6(1)
Ge	30(1)	50(7)	36(2)	57(4)	–	–	3.8(4)	19(1)	–
As	–	–	–	–	b.d.l.	7.1(24)	–	–	b.d.l.
Se	–	–	–	–	1121(105)	2436(354)	–	–	234(8)
Zr	414(20)	211(14)	44(2)	58(2)	141(8)	84(13)	934(36)	301(15)	1246(49)
Mo	19(1)	40(5)	41(2)	43(3)	–	–	21(4)	13(1)	–
Cd	–	–	–	–	782(55)	1470(437)	–	–	5158(238)
In	b.d.l.	0.61(5)	1.22(12)	–	311(20)	1012(226)	–	–	941(52)
Sn	0.13(1)	b.d.l.	b.d.l.	b.d.l.	0.11(1)	b.d.l.	b.d.l.	b.d.l.	0.16(3)
Sb	–	–	–	–	1.40(48)	33(8)	–	–	0.52(9)
Te	–	–	–	–	303(27)	1549(310)	–	–	40(4)
W	116(3)	145(13)	310(24)	192(10)	–	–	238(22)	181(24)	–
Pb	b.d.l.	0.32(7)	0.21(2)	0.26(3)	248(44)	611(207)	0.77(4)	0.16(2)	1534(61)

[a] Number of analyses [b] Number in brackets represent 2 SE in terms of least digits cited [c] b.d.l. = below detection limit [d] n.d. = not determined

Table S.2 Chemical compositions of metal phases determined by EPMA and LA-ICP-MS.

Run #	**PR1446**	**PR1449**	**PR1450**	**PR1465**	**PR1468**	**PR1470**	**PR1477**	**PR1480**	**PR1481**	**PR1489**	**PR1491**	**PR1505**	**PR1506**	**PR1508**
EPMA (wt.%)	*N = 30* [a]	*N = 29*	*N = 6*	*N = 45*	*N = 29*	*N = 30*	*N = 30*	*N = 12*	*N = 8*	*N = 25*	*N = 34*	*N = 27*	*N = 26*	*N = 12*
Fe	86.12(12)[b]	85.57(46)	82.98(157)	86.65(51)	85.77(42)	90.32(86)	84.92(64)	87.92(80)	92.00(35)	88.54(168)	85.56(101)	89.99(35)	91.60(33)	82.64(140)
Ni	5.13(4)	4.63(5)	5.21(21)	5.46(4)	4.89(6)	1.28(3)	5.09(6)	4.35(8)	0.67(2)	5.15(13)	5.83(11)	1.29(1)	1.47(1)	5.30(15)
Cr	b.d.l.	0.09(2)	0.08(3)	0.030(4)	0.039(8)	0.31(1)	0.07(1)	0.06(1)	0.28(2)	0.12(5)	0.07(3)	0.35(1)	0.16(1)	0.16(4)
Mo	–	–	–	–	–	1.73(28)	–	–	0.56(4)	–	–	1.88(13)	1.48(10)	–
W	–	–	–	–	–	1.29(5)	–	–	1.73(12)	–	–	1.43(4)	1.34(4)	–
P	–	–	–	–	–	1.31(44)	–	–	0.56(10)	–	–	1.16(14)	0.47(7)	–
Co	–	–	–	–	–	1.62(1)	–	–	1.16(3)	–	–	1.55(1)	1.76(1)	–
Ge	–	–	–	–	–	1.44(5)	–	–	0.45(4)	–	–	1.64(4)	1.43(2)	–
Mn	b.d.l.[c]	0.007(3)	b.d.l.	0.006(2)	0.004(2)	0.014(4)	0.006(3)	b.d.l.	0.03(1)	b.d.l.	0.004(2)	0.038(5)	0.01(1)	0.03(2)
V	–	–	–	–	–	0.038(4)	–	–	0.05(1)	–	–	0.054(5)	0.014(5)	–
In	0.51(1)	1.25(11)	0.85(28)	1.11(16)	0.82(10)	–	1.49(17)	1.16(18)	–	n.d.[d]	1.51(19)	–	–	1.46(17)
Cd	0.023(5)	0.59(9)	0.35(15)	0.16(4)	0.09(2)	–	0.53(9)	0.19(3)	–	0.07(7)	0.54(28)	–	–	0.06(7)
Sb	3.12(3)	2.00(12)	2.14(61)	1.84(15)	3.22(13)	–	2.27(15)	1.87(28)	–	n.d.	2.63(22)	–	–	2.46(23)
Pb	0.05(1)	1.09(12)	0.42(14)	0.17(5)	0.08(3)	–	0.65(12)	0.16(4)	–	0.23(15)	0.69(40)	–	–	0.36(8)
Se	0.08(1)	1.39(14)	1.24(45)	0.57(14)	0.90(19)	–	1.74(23)	0.70(13)	–	0.88(62)	0.69(16)	–	–	1.27(24)
Te	0.04(1)	0.80(8)	0.65(17)	0.21(5)	0.33(6)	–	0.96(12)	0.32(6)	–	n.d.	0.55(18)	–	–	0.58(11)
As	2.46(4)	1.29(3)	1.45(21)	1.11(9)	1.80(7)	–	1.42(6)	1.43(11)	–	1.63(23)	1.52(8)	–	–	1.58(7)
Total	97.55(9)	98.72(19)	95.37(50)	97.35(15)	97.98(25)	99.41(15)	99.19(15)	98.17(35)	97.54(19)	96.62(75)	98.61(28)	99.42(12)	99.75(21)	95.80(123)
LA-ICP-MS	*n.a.*[d]	*N = 9*	*N = 15*	*N = 13*	*N = 5*	*N = 12*	*N = 8*	*N = 9*	*n.a.*	*N = 12*	*N = 9*	*N = 9*	*N = 11*	*N = 12*
	–	–	–	–	–	*N (P) = 3*	–		–		–	*N (P) = 5*	*N (P) = 7*	–
P	–	–	–	–	–	10918(1295)	–	–	–	–	–	13949(863)	6193(646)	–
P_{corr} [e]	–	–	–	–	–	8953(1062)	–	–	–	–	–	11438(708)	5078(530)	–
V	–	–	–	–	–	192(21)	–	–	–	–	–	404(25)	134(67)	–
V_{corr}	–	–	–	–	–	269(29)	–	–	–	–	–	566(35)	188(94)	–
Cr	–	1268(89)	711(87)	315(35)	b.d.l.	2525(74)	309(64)	290(78)	–	774(122)	370(90)	3042(66)	1747(253)	1063(41)
Mn	–	114(26)	124(28)	24(4)	b.d.l.	343(29)	50(9)	68(17)	–	67(15)	40(8)	441(30)	240(39)	272(35)
Co	–	–	–	–	–	12712(205)	–	–	–	–	–	12715(89)	15203(389)	–
Ni	–	*Int.* [f]	*Int.*	*Int.*	*Int.*	*Int.*	*Int.*	*Int.*	–	*Int.*	*Int.*	*Int.*	*Int.*	*Int.*
Cu	–	71(2)	78(6)	78(4)	56(9)	60(3)	81(5)	86(9)	–	75(8)	82(3)	36(6)	34(2)	81(8)
Cu_{corr}	–	46(1)	51(4)	51(3)	36(6)	39(2)	52(3)	56(6)	–	49(5)	54(2)	23(4)	22(1)	53(5)
Zn	–	73(5)	85(9)	62(6)	165(85)	154(12)	142(15)	180(24)	–	112(18)	92(10)	74(7)	63(10)	137(14)
Zn_{corr}	–	18(1)	20(2)	15(1)	40(20)	37(3)	34(4)	43(6)	–	27(4)	22(2)	18(2)	15(2)	33(3)
Ga	–	2.7(2)	2.2(2)	3.0(2)	<9.4	3.8(6)	4.8(6)	5.8(12)	–	2.4(5)	2.9(2)	3.3(4)	2.4(4)	2.3(3)
Ga_{corr}		2.1(2)	1.7(2)	2.3(1)	<7.2	3.0(5)	3.7(5)	4.5(10)	–	1.9(4)	2.2(1)	2.6(4)	1.9(3)	1.8(3)
Ge	–	–	–	–	–	12597(332)	–	–	–	–	–	16489(333)	14692(209)	–
As	–	13230(253)	14432(442)	13608(637)	13097(2083)	51(6)	14846(349)	16327(497)	–	17206(1289)	17243(433)	–	–	15452(547)
Se	–	17769(1388)	21356(2920)	10099(1350)	15183(3200)	–	23092(1845)	16561(2316)	–	21523(4064)	8121(1273)	–	–	17486(2585)
Se_{corr}	–	12794(999)	15376(2102)	7271(972)	10932(2304)	–	16626(1328)	11924(1668)	–	15497(2926)	5847(917)	–	–	12590(1861)
Mo	–	–	–	–	–	10395(579)	–	–	–	–	–	13008(640)	10618(684)	–
Mo_{corr}	–	–	–	–	–	16424(915)	–	–	–	–	–	20553(1011)	16776(1081)	–
Cd	–	25976(3005)	43765(7114)	9424(1424)	11365(4681)	–	34171(5238)	39603(8860)	–	50440(14501)	12432(2267)	–	–	39404(13612)
Cd_{corr}	–	3637(421)	6127(996)	1319(199)	1591(655)	–	4784(733)	5544(1240)	–	7062(2030)	1740(317)	–	–	5517(1906)
In	–	20862(1952)	22917(3165)	24177(2871)	21530(4466)	<4.0	31838(2823)	38502(5140)	–	25128(3858)	23543(3193)	<1.7	b.d.l.	30525(4110)
In_{corr}	–	10222(956)	11229(1551)	11847(1407)	10550(2188)	<2.0	15601(1383)	18866(2519)	–	12313(1890)	11536(1565)	<0.8	–	14957(2014)
Sn	–	18(1)	8.5(8)	7.3(5)	17(6)	7.2(12)	11(1)	16(2)	–	4.6(9)	5.8(5)	5.0(7)	4.4(7)	5.2(8)
Sn_{corr}	–	13(1)	6.2(6)	5.4(4)	12(4)	5.3(9)	7.7(7)	11(2)	–	3.3(7)	4.3(4)	3.7(5)	3.2(5)	3.8(6)
Sb	–	23807(974)	23724(1859)	24868(1358)	29610(5986)	–	27637(1297)	24801(1264)	–	32642(3354)	33238(1197)	–	–	30724(1501)
Sb_{corr}	–	17617(721)	17556(1376)	18402(1005)	21911(4430)	–	20451(960)	18353(935)	–	24155(2482)	24595(886)	–	–	22736(1111)
Te	–	16413(1660)	24783(4312)	7093(985)	15621(4309)	–	27452(2769)	25082(5308)	–	25345(5433)	10141(1621)	–	–	28689(6495)
Te_{corr}	–	6401(647)	9665(1682)	2766(384)	6092(1681)	–	10706(1080)	9782(2070)	–	9885(2119)	3955(632)	–	–	11189(2533)
W	–	–	–	–	–	7717(606)	–	–	–	–	–	9374(397)	7768(447)	–
W_{corr}	–	–	–	–	–	13659(1073)	–	–	–	–	–	16592(703)	13749(791)	–

Pb	–	19735(2992)	19532(3407)	6337(894)	6137(2123)	15(2)	22135(3101)	21076(6781)	–	21352(6103)	9232(2050)	14(1)	5.3(11)	19408(6448)
Pb_{corr}	–	7104(1077)	7032(1227)	2281(322)	2209(764)	5.5(7)	7968(1116)	7587(2441)	–	7687(2197)	3323(738)	5.0(4)	1.9(4)	6987(2321)

Run #	**PR1510**	**PR1517**	**PR1518**	**PR1521**	**PR1522**	**PR1524**	**PR1538**	**PR1539**	**PR1561**
EPMA (wt.%)	*N = 29*	*N = 29*	*N = 32*	*N = 28*	*N = 30*	*N = 21*	*N = 29*	*N = 26*	*N = 30*
Fe	87.89(10)	89.18(28)	91.08(18)	89.66(22)	88.20(56)	82.38(136)	91.75(13)	91.19(22)	84.51(67)
Ni	0.79(1)	1.47(1)	1.43(1)	1.45(1)	5.25(4)	6.08(11)	1.39(2)	1.40(1)	5.04(5)
Cr	1.03(1)	0.82(1)	0.35(1)	0.79(1)	0.04(1)	0.04(1)	0.18(2)	0.37(1)	0.07(1)
Mo	1.27(4)	1.90(11)	1.44(7)	1.63(7)	–	–	1.44(6)	1.65(11)	–
W	1.44(3)	1.64(4)	1.42(3)	1.58(4)	–	–	1.51(3)	1.52(4)	–
P	0.11(1)	0.81(9)	0.78(7)	0.69(7)	–	–	0.50(5)	0.73(7)	–
Co	1.11(1)	1.76(1)	1.67(1)	1.75(1)	–	–	1.71(2)	1.70(1)	–
Ge	0.38(2)	1.47(3)	1.39(2)	1.67(2)	–	–	1.27(2)	1.36(2)	–
Mn	0.16(1)	0.14(1)	0.038(4)	0.11(1)	0.005(3)	0.004(3)	0.016(5)	0.04(5)	0.004(2)
V	0.29(1)	0.25(1)	0.030(5)	0.18(1)	–	–	0.029(5)	0.046(5)	–
In	–	–	–	–	1.11(15)	1.59(31)	–	–	1.47(14)
Cd	–	–	–	–	0.37(9)	0.27(8)	–	–	0.63(11)
Sb	–	–	–	–	2.00(13)	3.34(44)	–	–	2.01(15)
Pb	–	–	–	–	0.34(5)	0.43(12)	–	–	0.92(12)
Se	–	–	–	–	0.99(17)	0.61(17)	–	–	1.94(23)
Te	–	–	–	–	0.58(8)	0.46(10)	–	–	1.24(13)
As	–	–	–	–	1.40(5)	2.04(11)	–	–	1.40(3)
Total	94.48(9)	99.48(14)	99.68(10)	99.56(11)	100.30(11)	97.25(57)	99.82(11)	100.03(10)	99.26(13)
LA-ICP-MS	*N = 10*	*N = 11*	*N = 13*	*N = 12*	*N = 11*	*N = 11*	*N = 8*	*N = 9*	*N = 12*
	N (P) = 5	*N (P) = 5*	*N (P) = 6*	*N (P) = 4*	–	–	*N (P) = 5*	*N (P) = 6*	–
P	1562(117)	10455(575)	9540(576)	11572(950)	–	–	6785(634)	9352(956)	–
P_{corr}	1281(96)	8573(472)	7823(472)	9498(779)	–	–	5564(520)	7669(784)	–
V	1685(56)	2047(107)	363(62)	1763(110)	–	–	456(77)	392(77)	–
V_{corr}	2359(78)	2866(150)	508(87)	2468(154)	–	–	638(108)	549(108)	–
Cr	7516(168)	6882(128)	3287(136)	7411(214)	528(87)	440(85)	2156(205)	3540(199)	784(48)
Mn	1512(102)	1372(38)	571(105)	1436(99)	60(8)	44(11)	308(47)	563(62)	35(5)
Co	8759(59)	14623(85)	14015(106)	14117(146)	–	–	13931(192)	13777(166)	–
Ni	*Int.*	*Int.*	*Int.*	*Int.*	*Int.*	*Int.*	*Int.*	*Int.*	*Int.*
Cu	35(3)	29(1)	32(1)	29(5)	67(5)	89(4)	19(1)	28(4)	83(4)
Cu_{corr}	23(2)	19(1)	21(1)	19(3)	44(3)	58(3)	12(1)	18(3)	54(3)
Zn	50(11)	93(4)	98(9)	148(20)	125(14)	161(11)	53(4)	144(17)	69(4)
Zn_{corr}	13(3)	22(1)	24(2)	35(5)	30(3)	39(3)	13(1)	35(4)	17(1)
Ga	<2.4	2.6(3)	4.1(3)	<4.4	3.5(2)	3.6(4)	<3.4	b.d.l.	3.2(3)
Ga_{corr}	<1.8	2.0(3)	3.2(2)	<3.4	2.7(2)	2.8(3)	<2.7	–	2.5(3)
Ge	4251(33)	15182(195)	14009(187)	15672(196)	–	–	12974(412)	13796(437)	–
As	–	–	–	–	15346(484)	21271(740)	–	–	14800(296)
Se	–	–	–	–	13206(1871)	12077(976)	–	–	23399(1554)
Se_{corr}	–	–	–	–	9508(1347)	8695(703)	–	–	16847(1119)
Mo	4220(350)	13336(379)	12020(422)	10151(1338)	–	–	7495(937)	11845(1170)	–
Mo_{corr}	6668(553)	21071(599)	18992(667)	16039(2114)	–	–	11842(1480)	18720(1849)	–
Cd	–	–	–	–	21461(6954)	21584(2712)	–	–	32269(4170)
Cd_{corr}	–	–	–	–	3004(974)	3022(380)	–	–	4518(584)
In	0.47(13)	16(1)	14(1)	b.d.l.	20019(3469)	38271(3828)	b.d.l.	b.d.l.	27271(2248)
In_{corr}	0.23(6)	7.6(5)	6.9(5)	–	9809(1700)	18753(1876)	–	–	13363(1102)
Sn	1.94(4)	4.8(4)	7.2(9)	6.6(13)	6.8(4)	9.6(10)	3.8(8)	<10	7.4(4)
Sn_{corr}	1.42(29)	3.5(3)	5.3(7)	4.8(9)	5.0(3)	7.0(7)	2.8(6)	<7.3	5.4(3)
Sb	–	–	–	–	26073(1356)	45917(1558)	–	–	25315(713)
Sb_{corr}	–	–	–	–	19294(1003)	33979(1153)	–	–	18733(528)
Te	–	–	–	–	16828(5644)	15878(2017)	–	–	30756(3035)
Te_{corr}	–	–	–	–	6563(2201)	6192(787)	–	–	11995(1184)
W	2952(437)	10498(359)	9553(275)	6667(1073)	–	–	6272(656)	8151(408)	–

W_{corr}	5225(774)	18582(635)	16909(469)	11801(1899)	–	–	11101(1161)	14427(722)	–
Pb	2.4(2)	14(1)	8.9(14)	16(2)	15182(7155)	14518(2700)	5.9(10)	12(1)	22925(3563)
Pb_{corr}	0.86(7)	5.0(4)	3.2(5)	5.9(7)	5465(2576)	5227(972)	2.1(4)	4.5(3)	8253(1283)

[a] Number of analyses [b] Number in brackets represent 2 SE in terms of least digits cited [c] b.d.l. = below detection limit [d] n.a. = not analysed; n.d. = not determined [e] Calculated using correction factors listed in Table S1 [f] Used as internal standard for LA-ICP-MS data processing

Table S.3 Calculated maximum contribution (in %) of a CI- or H chondritic 0.02-0.05 mass% late veneer to the estimated lunar mantle abundances of volatile siderophile- and chalcophile elements

	Potential contribution (in %) to bulk silicate Moon abundances by delivery of CI chondrites	Potential contribution (in %) to bulk silicate Moon abundances by delivery of H chondrites
Cu	0.4–0.9	0.2–0.6
Zn	0.8–2.0	0.1–0.3
Ga	0.08–0.21	0.05–0.13
Ge	43–107	17–42
Se	17–42	6–16
Cd	1–3	0.02–0.05
In	1–2	0.2–0.5
Sn	1–2	0.4–1.1
Te	11–28	3–6
Pb	2–4	0.17–0.43